

Evaluation of the performance of non-hydrostatic RegCM4 (RegCM4-NH) over China

Thanh Nguyen-Xuan

The Hong Kong University of Science and Technology

Sze Lok Lam

The Hong Kong University of Science and Technology

Filippo Giorgi

Abdus Salam International Centre for Theoretical Physics

Erika Coppola

Abdus Salam International Centre for Theoretical Physics

Graziano Giuliani

Abdus Salam International Centre for Theoretical Physics

Xuejie Gao

Institute of Atmospheric Physics Chinese Academy of Sciences

Eun-Soon Im (✉ ceim@ust.hk)

Hong Kong University of Science and Technology <https://orcid.org/0000-0002-8953-7538>

Research Article

Keywords: Non-hydrostatic RegCM4, sensitivity of convective parameterization scheme, temperature and precipitation simulation in China

Posted Date: June 3rd, 2021

DOI: <https://doi.org/10.21203/rs.3.rs-550351/v1>

License:  This work is licensed under a Creative Commons Attribution 4.0 International License.

[Read Full License](#)

1 **Evaluation of the performance of non-hydrostatic RegCM4 (RegCM4-NH)**
2 **over China**

3 Thanh Nguyen-Xuan¹, Sze Lok Lam¹, Filippo Giorgi², Erika Coppola², Graziano Giuliani², Xuejie Gao³,
4 Eun-Soon Im^{1,4}

5 ¹Division of Environment and Sustainability, The Hong Kong University of Science and Technology, Hong Kong, China

6 ²Earth System Physics, Abdus Salam International Centre for Theoretical Physics, Trieste, Italy

7 ³Climate Change Research Center, Institute of Atmospheric Physics, Chinese Academy of Sciences, Beijing, China

8 ⁴Department of Civil and Environmental Engineering, The Hong Kong University of Science and Technology, Hong
9 Kong, China

10
11
12
13
14
15 **[Corresponding author]**

16 **Dr. Eun-Soon Im**

17 E-mail: ceim@ust.hk

18 Address: Academic Building 3594, The Hong Kong University of Science and Technology,
19 Clear Water Bay, Kowloon, Hong Kong, China.

22 **Abstract**

23 This study evaluates the performance of the latest version of non-hydrostatic RegCM4 (RegCM4-
24 NH) customized over two vast urban agglomerations in China (i.e., the Pearl River Delta, PRD, and
25 the Yangtze River Delta, YRD). The analysis focuses on how the dynamical core (hydrostatic versus
26 non-hydrostatic) employed in the driving mother domain simulation can affect the regional
27 characteristics of temperature and precipitation patterns in the PRD and YRD regions simulated by a
28 4 km resolution nested RegCM4-NH. In addition, we assess the sensitivity of the 4 km model results
29 to the use of a convective parameterization scheme (CPS), since the 4 km grid size can be considered
30 as a gray-zone resolution at which deep convection is partially resolved and may still need to be
31 parameterized. For mean temperature, a reasonable performance is shown by all simulations, with
32 the summer season mean bias mostly less than $\pm 1^\circ\text{C}$ when averaged over the PRD and YRD.
33 However, the simulated daily temperature distribution is excessively peaked around the median
34 value, indicating a large probability concentrated on a small temperature range. Although the higher
35 resolution slightly ameliorates this deficiency, the effect of the dynamical core and CPS tends to be
36 marginal. Conversely, precipitation behaves quite differently across simulations. The driving forcing
37 from the non-hydrostatic mother domain simulation helps to reduce a severe dry bias seen over the
38 PRD due to a reduction in convection inhibition. Use of the Emanuel CPS also tends to intensify
39 localized precipitation events over mountainous regions in connection with stronger ascending
40 motions over topographical features. The higher resolution also improves the phase of the diurnal
41 cycle of precipitation, both with and without the use of the CPS. In general, the performance of
42 RegCM4-NH over the PRD and YRD is found to be best when driven by a non-hydrostatic mother
43 domain simulation and when turning on the Emanuel CPS.

44 **Keywords:** Non-hydrostatic RegCM4, sensitivity of convective parameterization scheme,
45 temperature and precipitation simulation in China

46 **1. Introduction**

47 The Regional Climate Model version 4 (RegCM4) developed at the Abdus Salam International
48 Centre for Theoretical Physics (Pal et al. 2007; Giorgi 2012; Coppola et al. 2021) has been widely
49 applied across many regions worldwide for numerous purposes, ranging from process studies to
50 future projections. Almost all simulations using RegCM4 have been performed with a grid spacing
51 greater than 10 km because of the model's hydrostatic dynamical core. Recently, however, a non-
52 hydrostatic dynamics representation has been incorporated in the model (Coppola et al. 2021), which
53 has made it possible to carry out simulations at a few km resolution, i.e. in the so-called "convection
54 permitting (CP)" mode (e.g. Coppola et al. 2020; Ban et al. 2021; Pichelli et al. 2021). The advantage
55 of a non-hydrostatic core is that it is capable of explicitly resolving the vertical momentum equation
56 instead of using the hydrostatic approximation, and therefore allows the direct representation of
57 convection dynamics without the necessary use of convective parameterization schemes (CPS, e.g.,
58 Prein et al. 2015). It has been reported that regional climate models (RCMs) with non-hydrostatic
59 dynamical cores run in convection permitting mode, or CP-RCMs, better simulate the effects of
60 topography, boundary layer dynamics and timing of convection (Weisman et al. 1997; Hohenegger
61 et al. 2009; Prein et al. 2013; Prein et al. 2015; Fosser et al. 2015; Pontoppidan et al. 2017; Tan et al.
62 2018; Ban et al. 2021; Pichelli et al. 2021).

63 The first CP simulations using the RegCM4-NH over the European region are reported in Coppola et
64 al. (2020), Pichelli et al. (2021) and Ban et al. (2021), which highlight the model potential to better
65 simulate the local to regional climate characteristics at a very high resolution (i.e., 3 km). Motivated
66 by these results, here we investigate the transferability of RegCM4-NH over a portion of the China
67 territory. A conventional one-way double nesting technique is applied, employing a mother domain
68 with 20 km resolution and a nested domain with 4 km resolution. While the mother domain
69 encompasses most of the China territory, where climate is strongly influenced by the complex
70 interactions between surface heating, orography, and the East Asian summer monsoon (Ding 2013),

71 two nested domains focus on large urban agglomerations of China: the Pearl River Delta (PRD) and
72 Yangtze River Delta (YRD). These two regions are very likely to experience severe changes of
73 regional climate due to the acceleration of global warming and a rapid pace of urbanization. In this
74 regard, the need of high-resolution and high-quality climate simulations is particularly important in
75 order to simulate possible impacts of global warming (Qing and Wang 2021), for example related to
76 extreme heat stress exceeding a dangerous level. Our simulations also serve as a benchmark towards
77 the completion of experiments aimed at examining the effects of urban expansion in these areas
78 using the same modeling system with an improved urban module.

79 The horizontal resolution of 4 km employed for the nested domain is considered to some extent as a
80 so-called grey-zone resolution, at which convection is only partially resolved (Gerard 2007; Yu and
81 Lee 2010). In fact, although it has been argued that explicitly simulating convective systems requires
82 a grid size of less than 1 km (Craig and Dörnback 2008), some studies have shown that a larger grid
83 size (e.g., Li et al. (2020), up to 4.4 km) is still sufficient for the explicit simulation of convection
84 (Weisman et al. 1997; Prein et al. 2015; Scaff et al. 2020). Technically, there is ambiguity over what
85 resolution is sufficient, or needed, to resolve deep convection (Yu and Lee, 2010), and in particular,
86 the grid size of 4 km seems to be a boundary of whether the use of a CPS is necessary or not. For
87 example, focusing on the Guangdong-Hong Kong-Macao Greatest Bay area, one of our target
88 regions, Qing and Wang (2021) demonstrated that a horizontal grid spacing of 4 km yields
89 significant added value using the Weather Research and Forecasting (WRF) nesting system without
90 the use of the CPS. Yun et al. (2020) also showed an improved performance by a CP-scale
91 simulation over Eastern China using WRF with 3 km grid spacing.

92 Our study investigates the potential of CP simulations targeted over the PRD and YRD urban regions
93 using the RegCM4-NH, which, to the best of our knowledge, has not yet been applied and evaluated
94 over China. In order to assess the effect of using a CPS at 4 km grid spacing and to evaluate the
95 importance of the mother domain driving fields, we designed the set of experiments shown in Table

96 1, where either the hydrostatic or non-hydrostatic dynamical cores are used in the driving mother
97 domain, or a CPS is used or not. Although the mother domain's resolution (i.e., 20 km) allows the
98 use of the hydrostatic dynamical core, it is important to investigate the effect of the consistency of
99 dynamics representation between the mother and nested domains since, for example, the RegCM4-
100 NH was reported to perform better in capturing the characteristics of the Indian summer monsoon in
101 comparison to the hydrostatic model even at a resolution of 12 km (Maurya et al. 2020).

102 In addition to the RegCM4 experiments described in Table 1, for comparison purposes we carried
103 out WRF-based simulations with a CPS turned on and off using the same domain configuration (see
104 Table S1 and Table S2). Given that WRF has been extensively used for the simulation at CP scales,
105 this comparison gives us important insights into the behavior of the newly developed RegCM4-NH
106 over the East Asia region. The analysis focuses on the summer season (June-July-August: JJA) and
107 presents various statistical metrics ranging from seasonal mean to daily variability and the
108 precipitation diurnal cycle. The performance achieved in the CP simulation using the RegCM4-NH
109 will be a valuable reference for the RegCM modeling community.

110

111 **2. Experimental design**

112 **2.1. Model configuration and study area**

113 We use the RegCM-NH version 4.7 (hereafter referred to as RegCM4), which is the latest version
114 with the non-hydrostatic dynamical core and is described in Coppola et al. (2021). Figure 1
115 illustrates the topography used for the mother domain (hereafter referred to as D1) and two nested
116 domains (hereafter referred to as D2). While D1 covers the majority of China along with adjacent
117 countries (e.g., Korea, Japan) at a 20 km grid spacing, the two D2 cover the PRD and YRD regions,
118 respectively, with a grid spacing of 4 km. Fed by the higher resolution surface boundary conditions,
119 the nested domains exhibit more realistic topographical features than the mother domain. An

120 improved description of elevation gradient and the finer coastlines has proved to be essential in
121 generating more accurate meteorological information, thus leading to a clear added value of higher
122 resolution simulation (Qiu et al. 2020). In the vertical we use 23 and 41 levels for the mother and
123 nested domains, respectively.

124 Table 1 summarizes the two D1 and eight D2 experiments performed in this study. Each D2
125 simulation is driven by two D1 experiments using the hydrostatic and non-hydrostatic dynamical
126 core, respectively. In addition, for each D2 domain we run experiments with and without the CPS.
127 The integration spans the summer months (JJA) from 2011 to 2020 (10-years), with a one month
128 spin-up period. For the experiments with CPS we use the scheme of Emanuel (Emanuel and
129 Živković-Rothman 1999) based on several preliminary sensitivity experiments (not shown).
130 Compared to other schemes available in RegCM4, the Emanuel CPS exhibits the best performance
131 over our target region in terms of various metrics (e.g. bias and intensity distribution), which is
132 consistent with the results obtained from earlier RegCM4 simulations with coarse resolution (e.g.,
133 Gao et al. 2016; Nguyen-Xuan et al. 2020). Except for the CPS, all simulations share the same
134 physics parameterizations, i.e. the microphysics from Subgrid Explicit Moisture Scheme (SUBEX;
135 Pal et al. 2000), the planetary boundary layer parameterization based on Holtslag et al. (1990), the
136 radiative transfer scheme from the National Center for Atmospheric Research (NCAR) Community
137 Climate Model version 3 (CCM3) (Kiehl et al., 1996), land surface processes described by the
138 Community Land Model version 4.5 (CLM4.5) (Oleson and Lawrence 2013), and the ocean flux
139 scheme of Zeng et al. (1998).

140 Since the objective of this study is to investigate the performance of RegCM4-NH, the analysis
141 primarily focuses on the two nested domains (PRD and YRD), emphasizing the effect of the
142 dynamical core used in the driving D1 simulations and the effect of using the CPS. For validation,
143 we use the observational gridded dataset CN05 (Wu and Gao 2013), which was generated by
144 interpolation of more than 2400 in-situ data over China. This dataset includes both daily temperature

145 and precipitation at 25 km spatial resolution. For the model validation at sub-daily scale we use
146 observations from the Tropical Rainfall Measuring Mission (TRMM) 3B42 product with $0.25^\circ \times$
147 0.25° spatial resolution (Huffman et al. 2007).

148

149 **3. Results**

150 **3.1. Climatological pattern of summer temperature and precipitation**

151 We begin our analysis with the comparison of summer mean temperature averaged over the full 10-
152 year period (2000-2009) across all experiments of Table 1. Figure 2 shows the bias from two D1
153 simulations with the hydrostatic and non-hydrostatic dynamical core (hereafter referred to as D1-Hyd
154 and D1-NoHyd, respectively) and eight D2 simulations with different driving fields (i.e., D1-Hyd
155 and D1-NoHyd) and the Emanuel CPS turned on/off (i.e., D2-on and D2-off), against CN05
156 observation. The D1 simulations show a very similar bias pattern independent of their dynamical
157 core. The model tends to overestimate temperature over most of the northern parts of China and
158 underestimate it over southeastern China and the mountainous areas of northern Myanmar. These
159 results are in line with previous applications of the model (Gao et al. 2016; Gao et al. 2017).

160 For a more detailed comparison, Figure 2 shows results for the two D2 regions driven by the two D1
161 simulations. Over the PRD, D1-NoHyd shows slightly lower temperatures than D1-Hyd, but the
162 magnitude of the cold bias is mostly less than 1°C , which is a performance better than found in
163 previous papers using an earlier version of the model (e.g. Gao et al. 2016; Gao et al. 2017). An
164 interesting result is revealed by the comparison of the D2 simulations driven by D1-Hyd and D1-
165 NoHyd in that, in contrast to the bias patterns of the D1 experiments, the performance of the D2
166 simulation driven by D1-NoHyd is better than that driven by D1-Hyd. In fact, the effect of the
167 driving fields is more relevant than the effect of the CPS. Over the YRD the bias pattern is mixed,
168 with a warm bias in the north and a cold bias in the south. The D2 simulations amplify the warm bias

169 in the north but reduce the cold bias in the south noticeably, except for the region with higher
170 topography seen in Fig. 1 (c).

171 Figure 3 shows the same fields as Fig.2, but for precipitation. The CN05 observations show that the
172 summer precipitation is characterized by a strong regional variation. Due to the northward migration
173 of the monsoon rainband from southeastern China towards north China, Japan and the Korean
174 peninsula, maximum precipitation over these regions occurs in the mid to late summer season. The
175 D1 simulations show a wet bias in the northern part of the domain and a dry bias in the southern part.
176 Although both the D1-Hyd and D1-NoHyd exhibit a qualitatively similar bias pattern, the magnitude
177 of the wet bias is reduced in D1-NoHyd over a broad portion of the domain. This bias pattern
178 appears to be a systematic problem in RegCM4 simulations over this region, with similar errors
179 found in previous experiments (Gao et al. 2017).

180 Focusing on the D2 domains, the model performance is quite different between PRD and YRD
181 because the biases observed in the D1 simulations are essentially inherited by the D2 simulations.
182 The dry bias over PRD in the D1 simulations tends to be amplified in the D2 simulations,
183 particularly along the coastal regions. Conversely, the YRD simulations show relatively low biases.
184 Unlike temperature, the effect of the Emanuel CPS becomes noticeable in the precipitation bias from
185 the D2 simulations. If the CPS is active, the model tends to produce more precipitation, which in turn
186 helps to reduce the dry bias, in particular over the PRD region. The simulations driven by D1-NoHyd
187 produce further improvements in terms of reducing the dry bias for the PRD.

188 To assess the model performance more quantitatively, we present the joint distribution of summer
189 mean bias for temperature and precipitation averaged over the PRD and YRD for each of the 10
190 seasons (Fig. 4). Values close to zero indicate smaller magnitude biases. In addition to scatters, the
191 ellipses, which are derived from the multivariate t-distribution at a 0.9 confidence level, also help to
192 better illustrate the performance of individual simulations. For both regions, the consistency of the
193 dynamical core between D1 and D2 simulations is shown to have an impact on the bias pattern. The

194 D1-NoHyd and its downscaling results show a relatively smaller and less scattered bias pattern
195 compared to the D1-Hyd and its downscaling results. When the D2 simulations are driven by the D1-
196 NoHyd, the added value of higher resolution becomes clearer. More specifically, the downscaling
197 results of the D1-NoHyd consistently show a reduced size of the ellipses and scatter values closer to
198 the zero point for both the PRD and YRD regions, compared to the D2 runs driven by the D1-Hyd,
199 both with and without the CPS. When driven by the D1-NoHyd, the effect of the CPS is positive for
200 the PRD region, whereas its effect is less clear for the YRD region. In this region, the D1-NoHyd-
201 D2-off tends to expand the boundary of ellipse due to a few outlier values, but the biases for most
202 years are near the zero point.

203 In summary, based on the evaluation against the station-based observational data, both the D1 and
204 D2 simulations show a reasonable performance in terms of bias pattern for the climatological
205 summer mean temperature and precipitation in the PRD and YRD regions, despite with some
206 noticeable biases. In general, the range of biases seen in our simulations is comparable with previous
207 studies based on earlier versions of RegCM (e.g. Hui et al. 2015; Ji and Kang 2015; Gao et al. 2016;
208 Gao et al. 2017). The D2 simulations driven by D1-NoHyd tend to reduce the systematic biases
209 compared to those driven D1-Hyd. The use of the Emanuel CPS can contribute to a further reduction
210 of the dry bias, but its effect on temperature is marginal. Although the validation of climatological
211 seasonal mean patterns provides general indications of the performance of individual experiments,
212 the long-term average can conceal detailed behaviors. Therefore, the next section focuses on the
213 performance of daily temperature and precipitation in terms of frequency, intensity, and extremes.

214

215 **3.2. Analysis of daily temperature and precipitation**

216 Figure 5 presents the distribution of daily temperature and precipitation averaged over PRD and
217 YRD for the 10 simulated summer seasons. For each simulation, the plot displays the full actual

218 distribution smoothed by a kernel density estimator, which is useful for comparing the information of
219 the peak position and its relative amplitude across different simulations. In addition, conventional
220 box plots are also shown to provide information on basic statistics such as median, minimum,
221 maximum, and interquartile range.

222 For temperature, the statistics from the box-plots clearly demonstrate the added value of the D2
223 simulations compared to the D1. A common feature seen in PRD and YRD from the coarse
224 resolution simulations is an underestimate of the temperature variability, leading to a narrow
225 distribution, a problem which is improved by the higher resolution of D2. Conversely, the effect of
226 CPS and dynamical core of the driving runs does not seem to be relevant for the distribution of daily
227 temperature. Note that, although the D2 simulations are capable of providing improvements in mean
228 value and hot extremes, all simulations fail to reproduce accurately the shape of the observational
229 distribution, which is less peaked than in the models.

230 On the other hand, the Emanuel CPS significantly affects the model performance for daily
231 precipitation, thus leading to distinct distribution patterns. Without the CPS the simulated
232 distribution of daily precipitation shows a very different shape compared to the observed one, with a
233 much larger occurrence of weak intensity precipitation events. Use of the Emanuel CPS leads to a
234 flatter distribution, with a median value closer to the observed.

235 In summary, for both the PRD and YRD regions, the simulations with the Emanuel CPS show a
236 better performance in capturing the characteristics of the daily precipitation distribution. This result
237 differs from the findings of an earlier study that demonstrated the superiority of CP simulations at 4
238 km resolution over the PRD (e.g., Qing and Wang 2021). Evidently, this result depends also on the
239 different microphysics schemes used in the model. In addition, Qing and Wang (2021) obtained their
240 conclusion based on the comparison of a 4 km CP simulation with a 12 km simulation employing the
241 Kain-Fritsch CPS. Finally, note that while the effect of dynamical core of the D1 simulation is not as
242 important as the CPS over the YRD, the consistency of the dynamical core between the D1 and D2

243 simulations also tends to ameliorate the deficiency in the simulated precipitation distribution over
244 PRD.

245 To examine the characteristics of how daily precipitation is distributed with the temperature, Figure
246 6 shows the joint distribution of daily temperature and precipitation averaged over the PRD and
247 YRD. The shape of the distribution in PRD is more peaked and narrower than in YRD, and in this
248 regard all simulations are at least qualitatively compatible with the observed joint distributions. A
249 common feature in both regions is that temperature during intense precipitation is lower than during
250 the most frequent precipitation events, in particular over the PRD, where the intensity of heavy
251 precipitation is higher than in YRD. For the observational pattern in PRD, the peak of precipitation
252 occurrence is found around 28-29°C, whereas heavy precipitation above 100 mm/day occurs in the
253 temperature range of 24-25°C. While there is significant diversity in the performance of the different
254 simulations, the D2 experiments driven by D1-NoHyd show a better agreement with the observed
255 relationship between temperature and the frequency and intensity of daily precipitation. In particular,
256 the D1-NoHyd-D2-off shows a better distribution for both intensity and frequency of precipitation
257 for a given temperature interval compared with observations. Over the YRD, the shape of the
258 observed distribution is wide, i.e. precipitation occurs across a broad range of temperatures (e.g., 18-
259 33°C). In this region all simulations are able to capture the general pattern of the observed
260 distribution reasonably well.

261

262 **3.3. Analysis of the diurnal precipitation cycle**

263 The improvement of the precipitation diurnal cycle is one of the key aspects which is expected from
264 explicitly resolving convection (Ban et al. 2014; Li et al. 2020; Yun et al. 2020). Here, we compare
265 the performance of all simulations in capturing the phase and amplitude of precipitation diurnal cycle
266 averaged over the PRD and YRD regions (Fig. 7). For observational data, we use the TRMM 3B42

267 product at 3-hour intervals (Huffman et al. 2007) while the simulations are based on an hourly
268 precipitation output. To remove systematic mean biases and focus on the cycle itself, Figure 7
269 presents the anomaly of hourly precipitation (3-hourly for TRMM) with respect to the daily mean
270 value. The observations show a precipitation peak in the late afternoon over both PRD and YRD,
271 which was also found in Yun et al. (2020). While the phase of the cycle is similar in the two regions,
272 the amplitude is more pronounced in PRD than in YRD. The various simulations exhibit different
273 behaviours in terms of the shape and amplitude of the diurnal cycle. For both regions, the D1
274 simulations exhibit the correct amplitude but wrong phase of the cycle, with an earlier than observed
275 afternoon peak. This is a common behavior in hydrostatic models that utilize CPS (e.g. Ban et al.
276 2014; Prein et al. 2015; Im and Eltahir 2018). Conversely, the D2 simulations show a weakened
277 peak, particularly in the simulations without CPS, but a delayed timing of the peak, close to the
278 observed. The D1-Hyd and its downscaled counterpart tend to generate a bimodal shape of the
279 diurnal cycle with two peaks over the YRD region, which is less pronounced in the TRMM data. The
280 D2 simulation with CPS driven by D1-NoHyd shows slightly better performance compared to the
281 other simulations. This is an interesting result, as the Emanuel CPS appears to have a different
282 behavior when used within the high resolution CP simulation compared to the coarse resolution one.
283 In general, however, consistently with previous studies, the CP simulations are able to move the
284 diurnal precipitation peak forward in time, although the underestimate the amplitude of the daily
285 cycle.

286 Figure 8 shows the spatial distribution of the timing of the diurnal cycle peak from the TRMM
287 observation and all simulations. Consistently with Figure 7, the D1 simulations show a
288 systematically earlier peak across the entire PRD and YRD regions, while the D2 simulations exhibit
289 a spatial gradient of the peak timing and some significant spatial variability, which are much more
290 pronounced than in TRMM. This can be partly attributed to observational undersampling where
291 short-lived intensive rainfall could have been missed by the 3-h sampling period (Teo et al. 2011). In

292 addition, this spatial variability can at least partially contribute to the underestimation of the cycle's
293 magnitude when region averages are taken. The D2 simulations driven by the non-hydrostatic mother
294 domain simulation show the best agreement with observations. Also consistently with Figure 7, use
295 of the CPS does not affect strongly the phase of the peak, suggesting that the resolved component of
296 the convection mostly determines this aspect of the cycle.

297

298 **3.4. The physical mechanism behind the simulated bias patterns**

299 We now investigate the mechanisms behind the improvement found in the D1-NoHyd-D2-on
300 experiment, particularly in terms of reduction of the dry bias. First, we examine the atmospheric
301 thermodynamic structure, which directly leads to the suppression or enhancement of convective
302 activity. Figure 9 presents the vertically-integrated convective available potential energy (CAPE) and
303 convective inhibition (CIN) calculated from the daily data. Both indices are widely used as indicators
304 of atmospheric instability, but they serve different purposes. While the CAPE represents the positive
305 buoyancy of a rising air parcel, the CIN indicates the negative buoyant energy which prevents an air
306 parcel from ascending to the level of free convection (Rasmussen et al. 2017). This is manifested in
307 an inverse relationship between CAPE and CIN. Quantitatively, all D2 simulations with higher
308 resolution show larger CAPE than in the D1 simulations near the coastal regions where intense
309 precipitation occurs. At the same time, much lower CIN is found in regions with high CAPE.
310 Therefore the relatively large CAPE and small CIN observed in D1-NoHyd-D2-on generate
311 favourable conditions for reducing the model dry bias along the coasts of the PRD region.

312 For an in-depth analysis of how the CPS and dynamical core of the driving fields can control the
313 vertical thermodynamic structure related to CIN, we examine the Skew-T Log-P diagram, which
314 compares the slope of the adiabats and isotherms along the pressure levels, and thus is a measure of
315 static stability. Figure 10 illustrates the vertical profiles of temperature and dew point temperature

316 averaged over a small region in PRD (red box in Fig. 1b) along with the dry and moist adiabats. The
317 analysis is performed on July 2004, when all simulations exhibit an intense precipitation event. The
318 result is presented for a relatively low elevation level (between 750 and 1000 hPa) to focus on the
319 different behaviour across experiments in terms of lifting condensation level (LCL) and negative
320 energy area. The shaded area enclosed by the paths of adiabats and the environmental temperature
321 profile represents the magnitude of CIN, and its size indicates the amount of energy that is required
322 to lift the air parcel. Therefore, the simulation with a larger shaded area may need more energy to
323 overcome the negative buoyancy force, which is unfavorable for convection triggering. The D2
324 simulations driven by D1-Hyd show larger CIN than those driven by D1-NoHyd, and the
325 suppression of convection is more controlled by the driving dynamical core of the mother domain
326 than the CPS. In addition, the dynamical core of the mother domain leads to a systematic difference
327 in terms of the height of LCL, i.e. where a rising air parcel becomes saturated. In the D2 simulations
328 driven by D1-Hyd, the LCL is higher regardless of the use of the CPS, which is consistent with the
329 results showing a larger CIN eventually leading to drier conditions compared with the D2
330 simulations driven by D1-NoHyd.

331 Going back to the mean bias pattern of precipitation presented in Fig. 3 and spatial pattern of
332 vertically integrated CAPE and CIN in Fig. 9, the effect of the dynamical core seems to be marginal
333 in YRD, while it is important in PRD, while the CPS tends to reduce the dry bias. However, unlike
334 PRD, the similarity of CAPE and CIN spatial patterns in YRD may not provide a strong enough clue
335 to explain differences in precipitation biases resulting from the use of the CPS. Therefore, for the
336 YRD region, we analyze the processes related to the localized topographically-driven wet bias. For
337 this analysis, we select the target area outlined in Fig.1 (c) and investigate the latitudinal distribution
338 of precipitation along the terrain transects as well as the difference of vertical velocity (ω)
339 simulated with and without the CPS (Fig. 11). Since the wind penetrating over the area consistently
340 blows from the south to the north (Fig. 9), the zonal average along the latitudinal direction does not

341 induce a substantial smoothing of the variables analyzed. The zonal mean precipitation pattern is
342 clearly modulated by topography, following for example ridges and valleys evident in the south-
343 north transects of the nested domain. There is an important difference between the simulations using
344 the CPS, which tends to amplify the precipitation response to the orographic forcing and strengthen
345 the intensity of vertical motions. This is particularly the case for the D2 simulation driven by D1-
346 NoHyd.

347

348 **3.5. Comparison with WRF simulations**

349 For comparison purposes, we also carried out two different experiments using WRF as described in
350 Tables S1 and S2. The first WRF experiment (hereafter referred to as W-Exp1) adopts the one-way
351 double nesting technique and the same domain configuration as the RegCM4 experiments. The key
352 physics parameterizations of WRF are mostly the same as in the 3 km simulations of Yun et al.
353 (2020). In the second WRF experiment (hereafter referred to as W-Exp2) we adopt the two-way
354 double nesting capability of WRF and the physics parameterizations employed in Qian and Wang
355 (2021), who did not use any CPS over the PRD domain at 4 km resolution. However, since our
356 purpose for these experiments is to examine the effect of the CPS, we carried out two nested domain
357 simulations, one with and one without the Kain-Fritsch CPS. The reason behind our benchmarking
358 the experiments from Yun et al. (2020) and Qian and Wang (2021) is that they demonstrated the
359 great potential of convection permitting modeling around our target region. However, note that our
360 domain configuration and integration period are not the same as in Yun et al. (2020) and Qian and
361 Wang (2021).

362 Figures S1 and S2 present the bias pattern of JJA mean temperature and precipitation from 3-year
363 (2000-2002) simulations for the W-Exp1 and W-Exp2. In line with the RegCM4 results, for
364 precipitation the effect of the CP modeling framework emerges clearly when the CPS is used.

365 Turning off the CPS tends to increase the dry bias in both W-Exp1 and W-Exp2. Since W-Exp1
366 showed a better performance than W-Exp2 in terms of the bias pattern of JJA mean temperature and
367 precipitation (Figs. S1 and S2), we extended the integration period of W-Exp1 to 10-year (2000-
368 2009), which enables us to compare its statistics of daily temperature and precipitation with those
369 from the RegCM4 simulations.

370 Figure 12 presents the box plots of daily temperature and precipitation derived from D1-NoHyd and
371 its downscaled counterpart using RegCM4 and W-Exp1. For temperature in PRD, the WRF
372 simulations show a problem similar to that seen in the RegCM4 runs in terms of the shape of the
373 distribution, i.e. an excessively high probability density near the median value. In contrast to
374 RegCM4, the WRF simulation tends to produce excessively low extremes. In YRD, the deficiency in
375 the shape of the distribution is ameliorated in the WRF simulations, however a cold bias is still
376 evident, with both the median value and cold extremes being much lower than observed. Moving to
377 the precipitation in PRD, the WRF D2 simulation with CPS is in better agreement with the
378 observational shape of the distribution compared to D1-NoHyd-D2-on. However, the RegCM4 and
379 WRF simulations in YRD show a similar distribution shape, even though heavy precipitation from
380 WRF tends to be overestimated. Therefore, both models share some common behaviours, i.e. an
381 improvement of temperature in the nested domain simulations and an improvement of precipitation
382 in the simulation using the CPS.

383

384 **4. Discussion and conclusion**

385 In this study we examined the potential of RegCM4-NH to simulate the fine-scale climate
386 characteristics over the PRD and YRD regions of China. The implementation of the non-hydrostatic
387 dynamical core in the latest version of RegCM4 (Coppola et al. 2021) enables its use at very high
388 resolutions of up to a few km, which allows the model to resolve deep convection explicitly, instead

389 of parameterizing it. RegCM4-NH has already been used and evaluated mostly over the Europe
390 (Coppola et al. 2020; Pichelli et al. 2021; Ban et al. 2021), but not in other regions. Therefore, this
391 study presents a first analysis of the performance of RegCM4-NH over monsoon-dominated regions
392 of East Asia. Our target regions (PRD and YRD) are highly vulnerable to global warming and rapid
393 urbanization (Qing and Wang 2021), and especially the study of the latter will strongly benefit from
394 very high resolution.

395 Several recent studies have demonstrated the potential of CP simulations with grid spacing of 3-4 km
396 over parts of China using for example the WRF modeling system (e.g., Yun et al. 2020; Qing and
397 Wang 2021). However, a unique aspect of our study is that we tested the use of a CPS scheme at the
398 resolution of 4 km, which may still be considered as a gray zone resolution for which convection is
399 not fully represented. We thus tested the importance of using a CPS scheme in RegCM4-NH as well
400 as model driving fields derived from hydrostatic or non-hydrostatic simulations. For comparison, we
401 also completed a subset of analogous experiments with the WRF model.

402 Our analysis demonstrates that at 4 km resolution the use of the Emanuel CPS in RegCM4-NH
403 shows a better agreement with the observations in terms of daily temperature and precipitation
404 during the summer season over both our PRD and YRD target regions. In particular, turning on the
405 CPS contributes to a reduction of dry and cold biases. This finding is not consistent with some
406 previous studies that highlight the advantages of CP simulation at 4 km without use of a CPS (Qing
407 and Wang 2021), however, different RCM and domain configurations may explain this result.
408 Indeed, our WRF simulations also confirm that the performance in capturing daily precipitation
409 characteristics is better represented when using a CPS. However, the high resolution setting can lead
410 to an improvement of the phase of the diurnal cycle, both with and without the CPS, in line with
411 what found in previous studies.

412 It is worth noting that the SUBEX microphysics adopted in our RegCM4-NH runs may not be
413 optimal for explicitly describing convection due to its simplicity, and we are in the process of

414 evaluating more complex microphysics schemes. In addition, the Emanuel CPS has the limitation of
415 not including a separate parametrisation for shallow convection, which is often needed to trigger
416 convection in the CP setting. Additionally, our results indicate that the dynamical core employed in
417 the mother domain simulation can affect the performance of the nested domain experiment.
418 Specifically, the consistency of dynamical cores between the nested and mother domain simulations
419 tends to reduce the model biases. The effects of CPS and dynamical core of the mother domain
420 depends on the region.

421 The statistical metrics used to evaluate the model performance were based on the use of the CN05
422 observational data, whose resolution (25 km) is appropriate for the validation of mother domain
423 simulation (20 km grid spacing) but less so to demonstrate the added value of the high resolution of
424 the nested domain simulation. Despite this shortcoming, the 4 km RegCM4-NH simulations showed
425 a promising performance over these regions of China, in line with the performance of the WRF
426 model, and thus can provide a useful tool to study regional-to-local climate in East Asia.

427

428 **Funding**

429 Im E.-S., Nguyen-Xuan T., and Lam S.-L. were supported by the Hong Kong Research Grants
430 Council funded project (ECS26309618).

431 **Conflicts of interest**

432 The authors declare no competing interests.

433 **Availability of data and material**

434 All simulation data will be made available on reasonable request.

435 **Code availability**

436 R and GrADS scripts and Fortran code used for the analysis are available from the corresponding
437 author upon reasonable request.

438 **References**

- 439 Ban N, Caillaud C, Coppola E et al. (2021) The first multi-model ensemble of regional climate simulations at
440 kilometer scale resolution, part I: evaluation of precipitation. *Clim Dyn.* [https://doi.org/10.1007/s00382-](https://doi.org/10.1007/s00382-021-05708-w)
441 [021-05708-w](https://doi.org/10.1007/s00382-021-05708-w)
- 442 Ban N, Schmidli J, and Schär C (2014) Evaluation of the convection-resolving regional climate modeling
443 approach in decade-long simulations, *J. Geophys. Res. Atmos.*, 119, 7889–7907,
444 doi:10.1002/2014JD021478.
- 445 Coppola E, Sobolowski S, Pichelli E et al. (2020) A first-of-its-kind multi-model convection permitting
446 ensemble for investigating convective phenomena over Europe and the Mediterranean. *Clim Dyn* 55:3–
447 34. <https://doi.org/10.1007/s00382-018-4521-8>
- 448 Coppola, E., Stocchi, P., Pichelli, E., Torres Alavez, J. A., Glazer, R., Giuliani, G., Di Sante, F., Nogherotto,
449 R., and Giorgi, F.: Non-Hydrostatic RegCM4 (RegCM4-NH): Model description and case studies over
450 multiple domains, *Geosci. Model Dev. Discuss.* [preprint], <https://doi.org/10.5194/gmd-2020-435>, in
451 review, 2021.
- 452 Craig GC and Dörnbrack A (2008) Entrainment in Cumulus Clouds: What Resolution is Cloud-Resolving?
453 *Journal of the Atmospheric Sciences* 65(12):3978-3988. <https://doi.org/10.1175/2008JAS2613.1>
- 454 Ding Y-H (2013) *China climate*. China Science Press, Beijing
- 455 Emanuel KA and Živković-Rothman M (1999) Development and evaluation of a convection scheme for use in
456 climate models. *Journal of the Atmospheric Sciences* 56(11):1766-1782. [https://doi.org/10.1175/1520-](https://doi.org/10.1175/1520-0469(1999)056<1766:DAEOAC>2.0.CO;2)
457 [0469\(1999\)056<1766:DAEOAC>2.0.CO;2](https://doi.org/10.1175/1520-0469(1999)056<1766:DAEOAC>2.0.CO;2)
- 458 Fosser G, Khodayar S, Berg P (2015) Benefit of convection permitting climate model simulations in the
459 representation of convective precipitation. *Clim Dyn* 44(1–2):45–60
- 460 Gao X, Shi Y, Giorgi F (2016) Comparison of convective parameterizations in RegCM4 experiments over
461 China with CLM as the land surface model. *Atmospheric and Oceanic Science Letters* 9(4):246-254.
462 <https://doi.org/10.1080/16742834.2016.1172938>
- 463 Gao X, Shi Y, Han Z et al. (2017) Performance of RegCM4 over major river basins in China. *Adv. Atmos.*
464 *Sci.* 34:441–455. <https://doi.org/10.1007/s00376-016-6179-7>
- 465 Gerard L (2007) An integrated package for subgrid convection, clouds and precipitation compatible with
466 meso-gamma scales. *Q. J. R. Meteorol. Soc.* 133:711–730. <https://doi.org/10.1002/qj.58>
- 467 Giorgi F, Coppola E, Solmon F et al. (2012) RegCM4: Model description and preliminary tests over multiple
468 CORDEX domains. *Climate Research* 52:31–48.
- 469 Hohenegger C, Brockhaus P, Bretherton CS, Schär C (2009) The soil moisture-precipitation feedback in
470 simulations with explicit and parameterized convection. *J Clim* 22:5003–5020
- 471 Holtslag A, Bruijn ED, and Pan H (1990) A High Resolution Air Mass Transformation Model for Short-range
472 Weather Forecasting. *Monthly Weather Review* 118:1561–1575.

473 Huffman GJ et al (2007) The TRMM multisatellite precipitation analysis (TMPA): quasi-global, multiyear,
474 combined-sensor precipitation estimates at Fine Scales. *J Hydrometeorol* 8:38–55

475 Hui P, Tang J, Wang S, and J Wu (2015) Sensitivity of simulated extreme precipitation and temperature to
476 convective parameterization using RegCM3 in China. *Theor Appl Climatol* 122: 315-335.

477 Im ES, Eltahir EAB (2018) Simulation of the diurnal variation of rainfall over the western Maritime Continent
478 using a regional climate model. *Clim Dyn* 51:73–88.

479 Ji Z, and Kang S (2015) Evaluation of extreme climate events using a regional climate model for China. *Int. J.*
480 *Climatol.* 35: 888-902.

481 Kiehl J, Hack J, Bonan G, Boville B, Williamson D, and Rasch P (1998) The National Center for Atmospheric
482 Research Community Climate Model: CCM3. *Journal of Climate* 11:1131–1149.

483 Li P, Furtado K, Zhou T et al. (2020) The diurnal cycle of East Asian summer monsoon precipitation
484 simulated by the Met Office Unified Model at convection-permitting scales. *Clim Dyn* 55:131–151.
485 <https://doi.org/10.1007/s00382-018-4368-z>

486 Maurya RKS, Mohanty MR, Sinha P, Mohanty UC (2020) Performance of hydrostatic and non-hydrostatic
487 dynamical cores in RegCM4.6 for Indian summer monsoon simulation. *Meteorological Application*
488 27(3). <https://doi.org/10.1002/met.1915>

489 Nguyen-Xuan T, Qiu L, Im ES, Hur J, Shim KM (2020) Sensitivity of summer precipitation over Korea to
490 convective parameterizations in the RegCM4: An updated assessment. *Advances in Meteorology* 2020.
491 <https://doi.org/10.1155/2020/1329071>

492 Oleson KW and Lawrence DM (2013) Technical Description of Version 4.5 of the Community Land Model
493 (CLM). NCAR Technical Note NCAR/TN-503+STR, NCAR, Boulder, CO, USA.

494 Pal JS, Giorgi F, Bi X et al. (2007) The ICTP RegCM3 and RegCNET: Regional climate modeling for the
495 developing world. *Bulletin of the American Meteorological Society* 88(9):1395–1410.
496 <https://doi.org/10.1175/BAMS-88-9-1395>

497 Pal JS, Small EE, Eltahir EAB (2000) Simulation of regional-scale water and energy budgets: Representation
498 of subgrid cloud and precipitation processes within RegCM. *Journal of geophysical research*
499 105(D24):29579-29594.

500 Pichelli E, Coppola E, Sobolowski S et al. (2021) The first multi-model ensemble of regional climate
501 simulations at kilometer-scale resolution part 2: historical and future simulations of precipitation. *Clim*
502 *Dyn.* <https://doi.org/10.1007/s00382-021-05657-4>

503 Pontoppidan M, Reuder J, Mayer S and Kolstad EW (2017) Downscaling an intense precipitation event in
504 complex terrain: the importance of high grid resolution. *Tellus A: Dynamic Meteorology and*
505 *Oceanography* 69(1):1271561.

506 Prein AF, Langhans W, Fosser G, Ferrone A, Ban N, Goergen K, Keller M, Tölle M, Gutjahr O, Feser F,
507 Brisson E, Kollet S, Schmidli J, van Lipzig NPM, Leung R (2015) A review on regional convection-
508 permitting climate modeling: Demonstrations, prospects, and challenges. *Rev. Geophys.* 53:323–361.
509 <https://doi.org/10.1002/2014RG000475>

510 Prein F, Gobiet A, Suklitsch M, Truhetz H, Awan NK, Keuler K, Georgievski G (2013) Added value of
511 convection permitting sea-sonal simulations. *Clim Dyn* 41(9–10):2655–2677

512 Qing Y, Wang S (2021) Multi-decadal convection-permitting climate projections for China’s Greater Bay
513 Area and surroundings. *Clim Dyn*. <https://doi.org/10.1007/s00382-021-05716-w>

514 Qiu L, Im ES, Hur J, Shim KM (2020) Added value of very high resolution climate simulations over South
515 Korea using WRF modeling system. *Clim Dyn* 54:173–189. <https://doi.org/10.1007/s00382-019-04992-x>

516 Rasmussen KL, Prein AF, Rasmussen RM, Ikeda K, and Liu C (2017) Changes in the convective population
517 and thermodynamic environments in convection-permitting regional climate simulations over the United
518 States. *Clim Dyn* 55:383–408. <https://doi.org/10.1007/s00382-017-4000-7>

519 Scaff L, Prein AF, Li Y et al (2020) Simulating the convective precipitation diurnal cycle in North America’s
520 current and future climate. *Clim Dyn* 55:369–382. <https://doi.org/10.1007/s00382-019-04754-9>

521 Tan H, Ray P, Barrett BS, Tewari M, Moncrieff MW (2020) Role of topography on the MJO in the maritime
522 continent: a numerical case study. *Clim Dyn* 55:295–314. <https://doi.org/10.1007/s00382-018-4275-3>

523 Teo CK, Koh TY, Lo JCF, Bhatt BH (2011) Principal component analysis of observed and modeled diurnal
524 rainfall in the Maritime Continent. *J Clim* 24:4662–4675

525 Weisman ML, Skamarock WC, Klemp JB (1997) The resolution dependence of explicitly modeled convective
526 systems. *Mon Weather Rev* 125(4):527–548

527 Wu J and Gao X (2013) A gridded daily observation dataset over China region and comparison with other
528 datasets. *Chinese J. Geophys-CH* 56:1102-1111.

529 Yu X and Lee TY (2010) Role of convective parameterization in simulations of a convection band at grey-
530 zone resolutions. *Tellus A* 62:617-632. <https://doi.org/10.1111/j.1600-0870.2010.00470.x>

531 Yun Y, Liu C, Luo Y et al. (2020) Convection-permitting regional climate simulation of warm-season
532 precipitation over Eastern China. *Clim Dyn* 54:1469–1489. <https://doi.org/10.1007/s00382-019-05070-y>

533 Zeng X, Zhao M, and Dickinson RE (1998) Intercomparison of bulk aerodynamic algorithms for the
534 computation of sea surface fluxes using TOGA COARE and TAO data. *Journal of Climate* 11(10):2628–
535 2644.

536

537

538

539

540

541

542

543

544

545

546

547 **Table List**

548

549 Table 1. Summary of experimental design performed in this study using RegCM4.

550

551 **Figure List**

552 **Fig. 1.** Domain and topography used for the (a) mother domain and (b, c) two nested domains
553 simulations. The geographical locations of two nested domains are marked by red line
554 rectangles in the mother domain. The areas of red line rectangle in (b) and (c) are selected for
555 in-depth analysis presented in Fig. 8 and Fig. 9, respectively.

556 **Fig. 2.** The spatial distributions of (I) JJA mean temperature (unit: °C) from CN05 observation and
557 the bias of JJA mean temperature from (II) D1-Hyd and (III) D1-NoHyd over the whole
558 domain, and the bias of JJA mean temperature over (d-g) PRD and (k-n) YRD from two
559 nested domain simulations with the Emanuel CPS turn on/off driven by (d, e, k, l) D1-Hyd
560 and (f, g, m, n) D1-NoHyd during the 10-year period (2000-2009). The distributions
561 presented in (I), (II), and (II) are zoomed up with respect to (a-c) PRD and (h- j) YRD to
562 facilitate clear comparison with the nested domain simulations.

563 **Fig. 3.** Same as Fig. 2, expect for JJA mean precipitation (unit: mm/day).

564 **Fig. 4.** The scatter plot of area-averaged bias of JJA mean temperature and precipitation over (a, b)
565 PRD and (c, d) YRD on a yearly basis. The results from D1-Hyd (D1-NoHyd) and its
566 downscaling simulations are marked as circle (triangle). The ellipses with three different
567 colors indicate the multivariate t-distribution at 0.9 confidence level that is calculated from
568 the corresponding data with the same color.

569 **Fig. 5.** Violin (shaded) and box plots of (a, c) daily temperature and (b, d) daily precipitation
570 averaged over (a, b) PRD and (c, d) YRD. The y-axis for (b, d) daily precipitation was
571 square-root transformed for better visualization.

572 **Fig. 6.** Joint probability distribution of daily temperature and daily precipitation averaged over (a)
573 PRD and (b) YRD. The different color is proportional to the percentage of corresponding
574 days.

575 **Fig. 7.** Anomalous diurnal variation of precipitation rate averaged over the PRD and YRD derived
576 from TRMM 3-hour observation and 1-hour output of all simulations. Anomalous value at
577 each time is computed by subtracting daily mean value. The x-axis indicates the local solar
578 time (LST). The TRMM observation marked by black line is the same in all six panels for (a)
579 PRD and (b) YRD, respectively.

580 **Fig. 8.** The peak timing in the diurnal cycle of precipitation derived from the TRMM observation (a)
581 and all simulations (b-g) for (I) PRD and (II) YRD, respectively.

582 **Fig. 9.** The spatial distribution of vertically accumulated (a-g) CAPE and (h-m) CIN over (I) PRD
583 and (II) YRD. JJA mean wind vectors are overlaid in the distribution of CAPE.

584 **Fig. 10.** Skew-T Log-P diagram showing the vertical structure of temperature (T) and dew point
585 temperature (Td) averaged over rectangle in Fig. 1 (b) on July, 2004. While the red and
586 orange solid lines indicate T and Td, respectively, the green, blue and purple dashed lines
587 indicate dry adiabat, moist adiabat, and mixing ratio, respectively. The red dot indicates the
588 lifting condensation level and the shaded area is equivalent to the magnitude of CIN.

589 **Fig. 11.** (a, b, d, e) Latitudinal distribution of precipitation (blue line, unit: mm/day) zonally
590 averaged over 120.86E-121.4E (Fig. 1c) along the south-north topographical transects (grey
591 shading) and (c, f) vertical structure of omega difference (unit: Pa/s) between simulations
592 with CPS on and off.

593 **Fig. 12.** Violin (shaded) and box plots of (a, c) daily temperature and (b, d) daily precipitation
594 averaged over the PRD and YRD. The y-axis for (b, d) daily precipitation was square-root
595 transformed for better visualization. The distributions of CN05, D1-NoHyd, D1-NoHyd-D2-
596 off, and D1-NoHyd-D2-on are the same with those from Fig. 5.

597

598

599

600

601

602

603

604

605

606

607

608

609

610

611

612

613

614

615 **Table 1.** Summary of experimental design performed in this study using RegCM4.
 616

Name	Area	Grid size	Dynamic core	Emanuel CPS	Shared configuration
D1-Hyd	East Asia	20 km	Hydrostatic	On	<ul style="list-style-type: none"> - PBL: Holtslag - Microphysics: SUBEX - Land surface model: CLM4.5 - Radiation: CCM3
D1-Hyd-D2-off	PRD & YRD	4 km	Non-hydrostatic	Off	
D1-Hyd-D2-on	PRD & YRD	4 km	Non-hydrostatic	On	
D1-NoHyd	East Asia	20 km	Non-hydrostatic	On	
D1-NoHyd-D2-off	PRD & YRD	4 km	Non-hydrostatic	Off	
D1-NoHyd-D2-on	PRD & YRD	4 km	Non-hydrostatic	On	

617

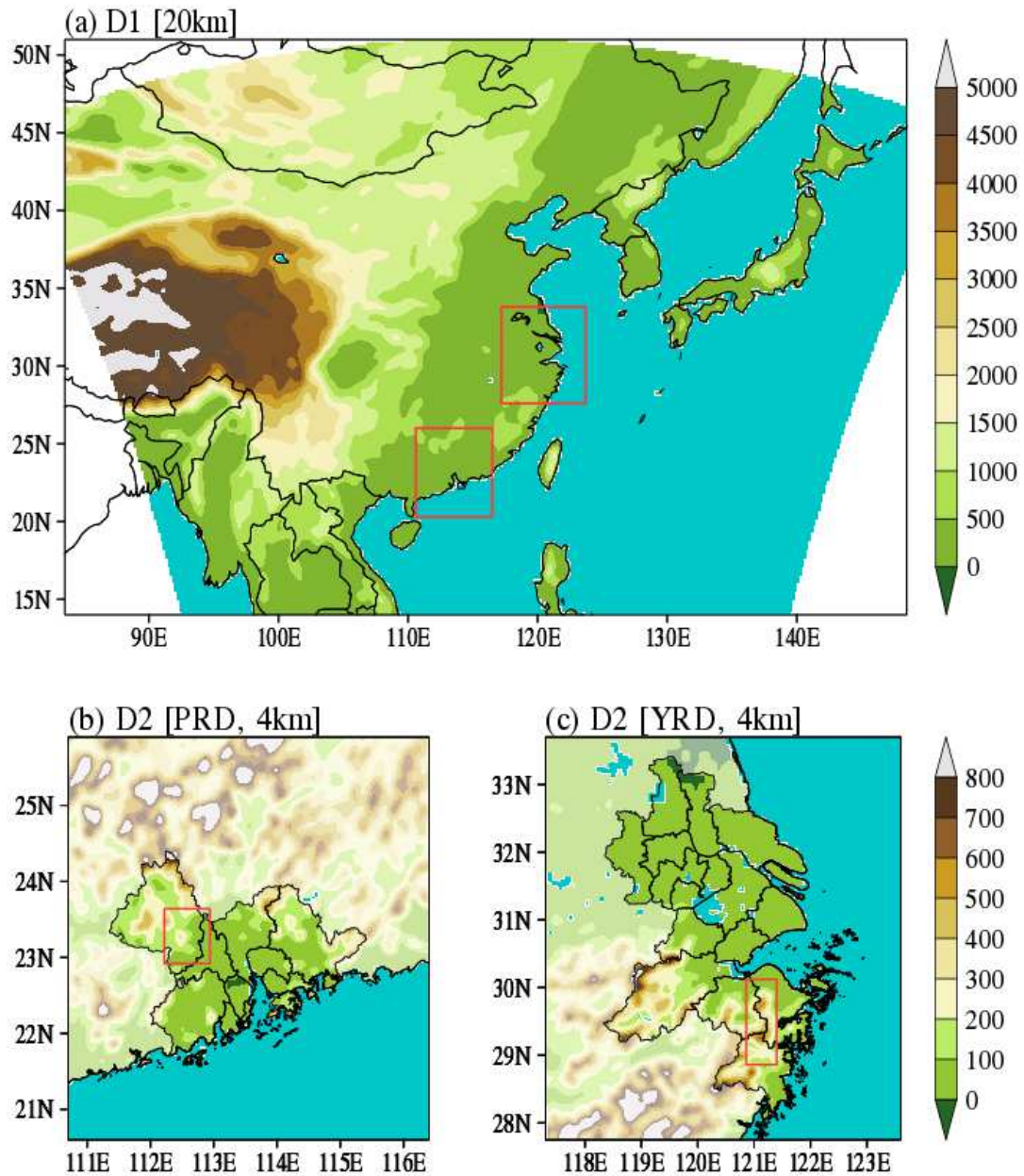


Fig. 1. Domain and topography used for the (a) mother domain and (b, c) two nested domains simulations. The geographical locations of two nested domains are marked by red line rectangles in the mother domain. The areas of red line rectangle in (b) and (c) are selected for in-depth analysis presented in Fig. 8 and Fig. 9, respectively.

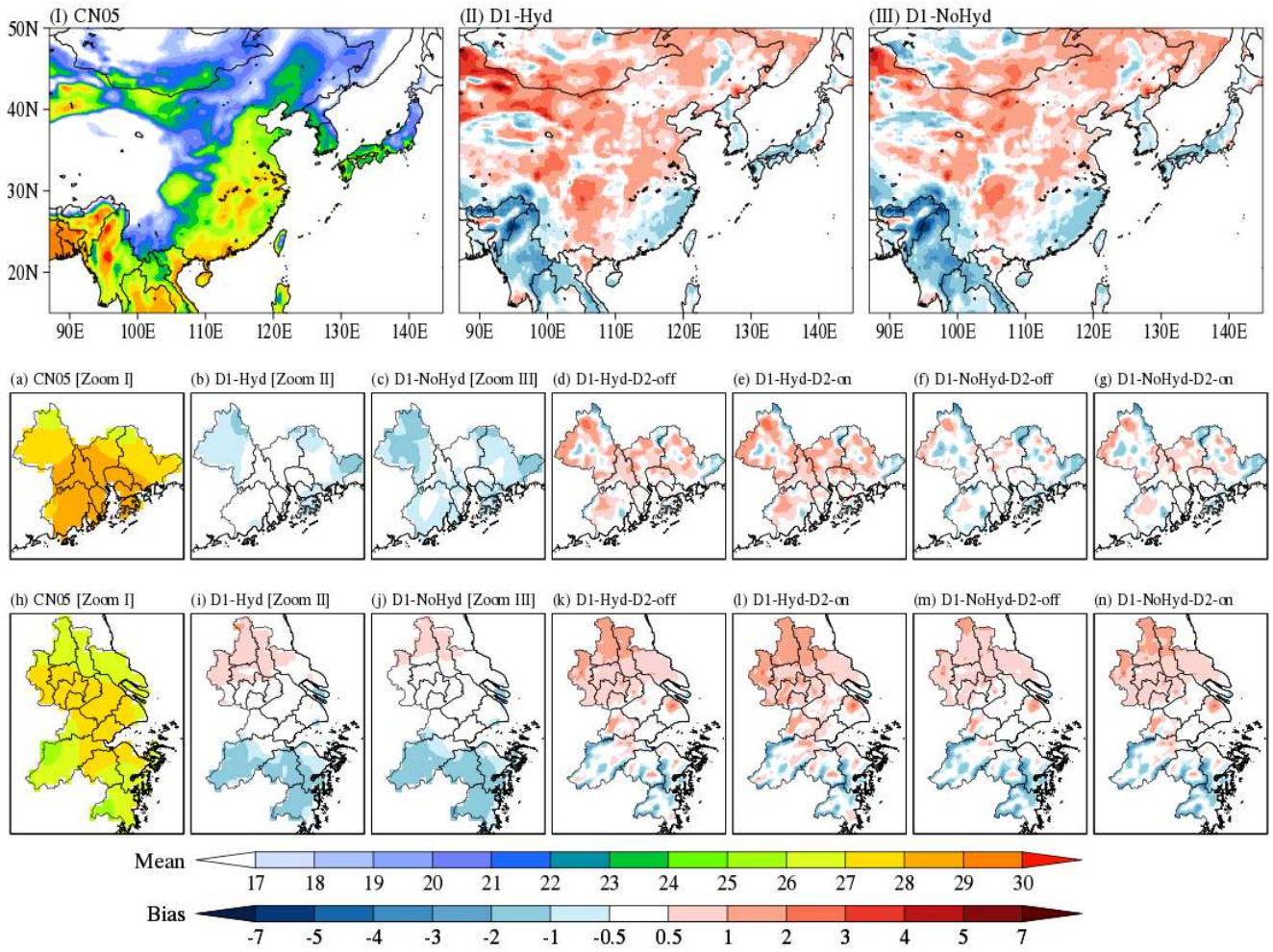


Fig. 2. The spatial distributions of (I) JJA mean temperature (unit: °C) from CN05 observation and the bias of JJA mean temperature from (II) D1-Hyd and (III) D1-NoHyd over the whole domain, and the bias of JJA mean temperature over (d-g) PRD and (k-n) YRD from two nested domain simulations with the Emanuel CPS turn on/off driven by (d, e, k, l) D1-Hyd and (f, g, m, n) D1-NoHyd during the 10-year period (2000-2009). The distributions presented in (I), (II), and (II) are zoomed up with respect to (a-c) PRD and (h- j) YRD to facilitate clear comparison with the nested domain simulations.

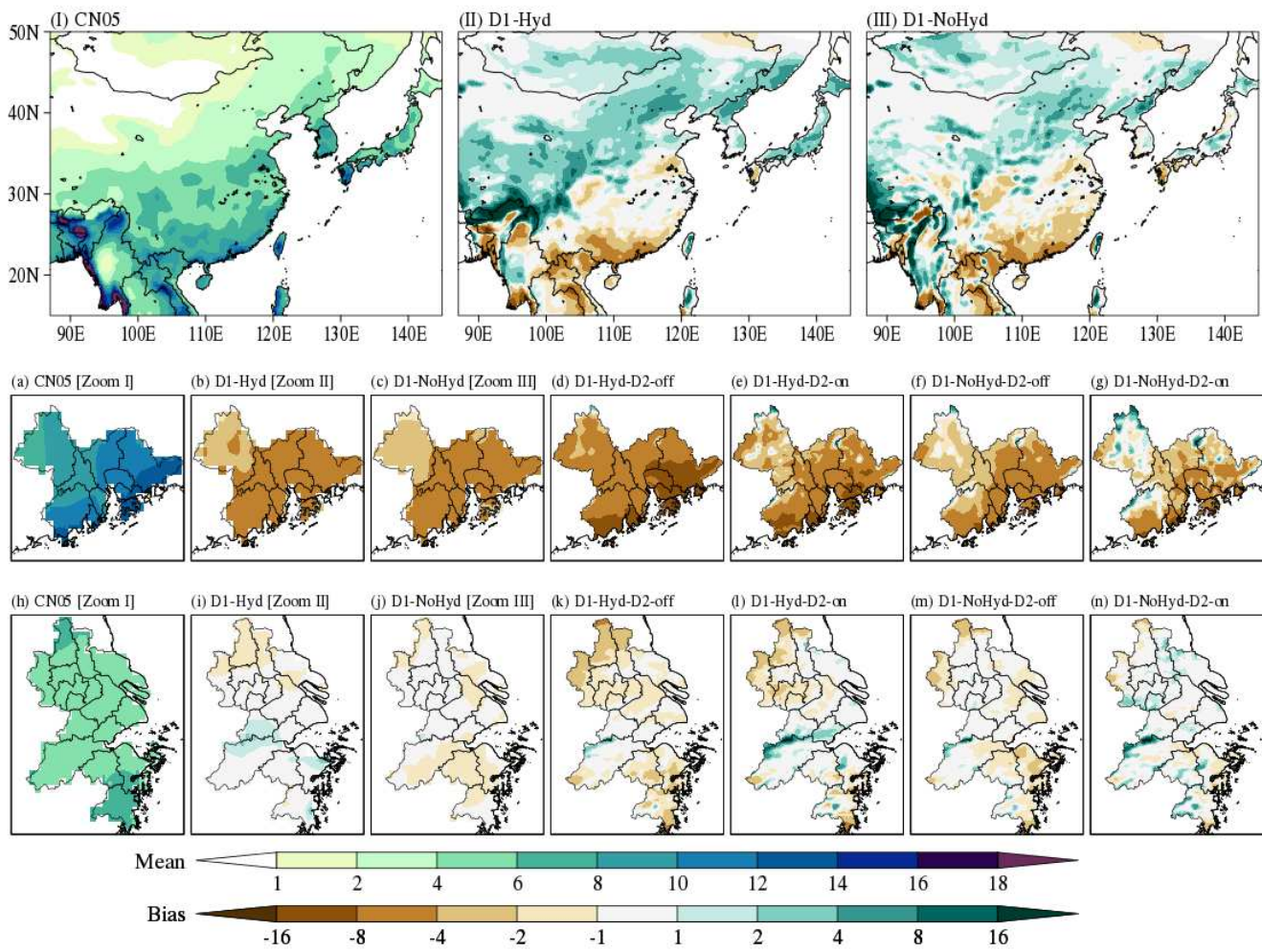
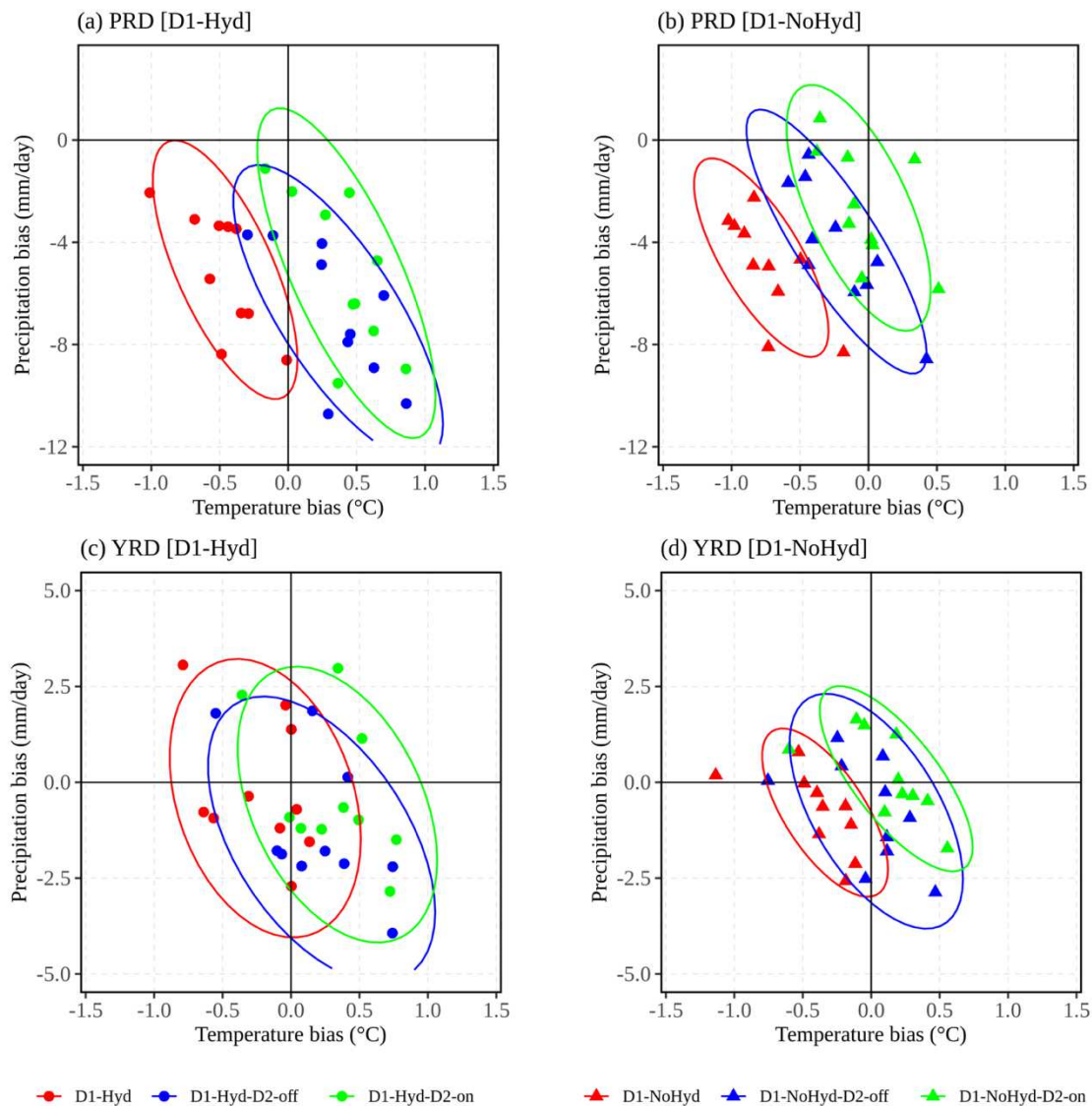


Fig. 3. Same as Fig. 2, expect for JJA mean precipitation (unit: mm/day).

620



The ellipses is based on the multivariate t -distribution (confidence level=0.9)

Fig. 4. The scatter plot of area-averaged bias of JJA mean temperature and precipitation over (a, b) PRD and (c, d) YRD on a yearly basis. The results from D1-Hyd (D1-NoHyd) and its downscaling simulations are marked as circle (triangle). The ellipses with three different colors indicate the multivariate t -distribution at 0.9 confidence level that is calculated from the corresponding data with the same color.

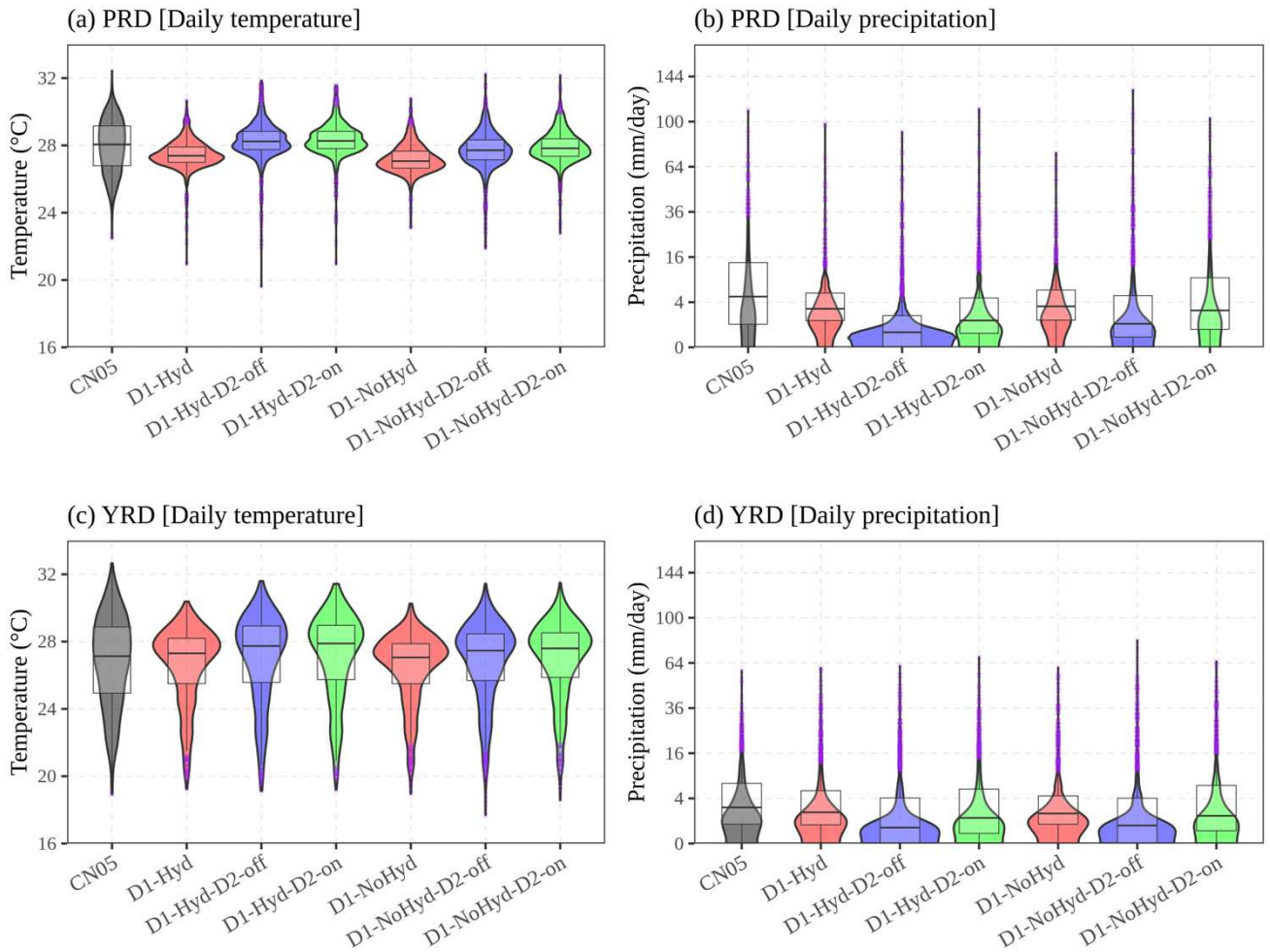


Fig. 5. Violin (shaded) and box plots of (a, c) daily temperature and (b, d) daily precipitation averaged over (a, b) PRD and (c, d) YRD. The y-axis for (b, d) daily precipitation was square-root transformed for better visualization.

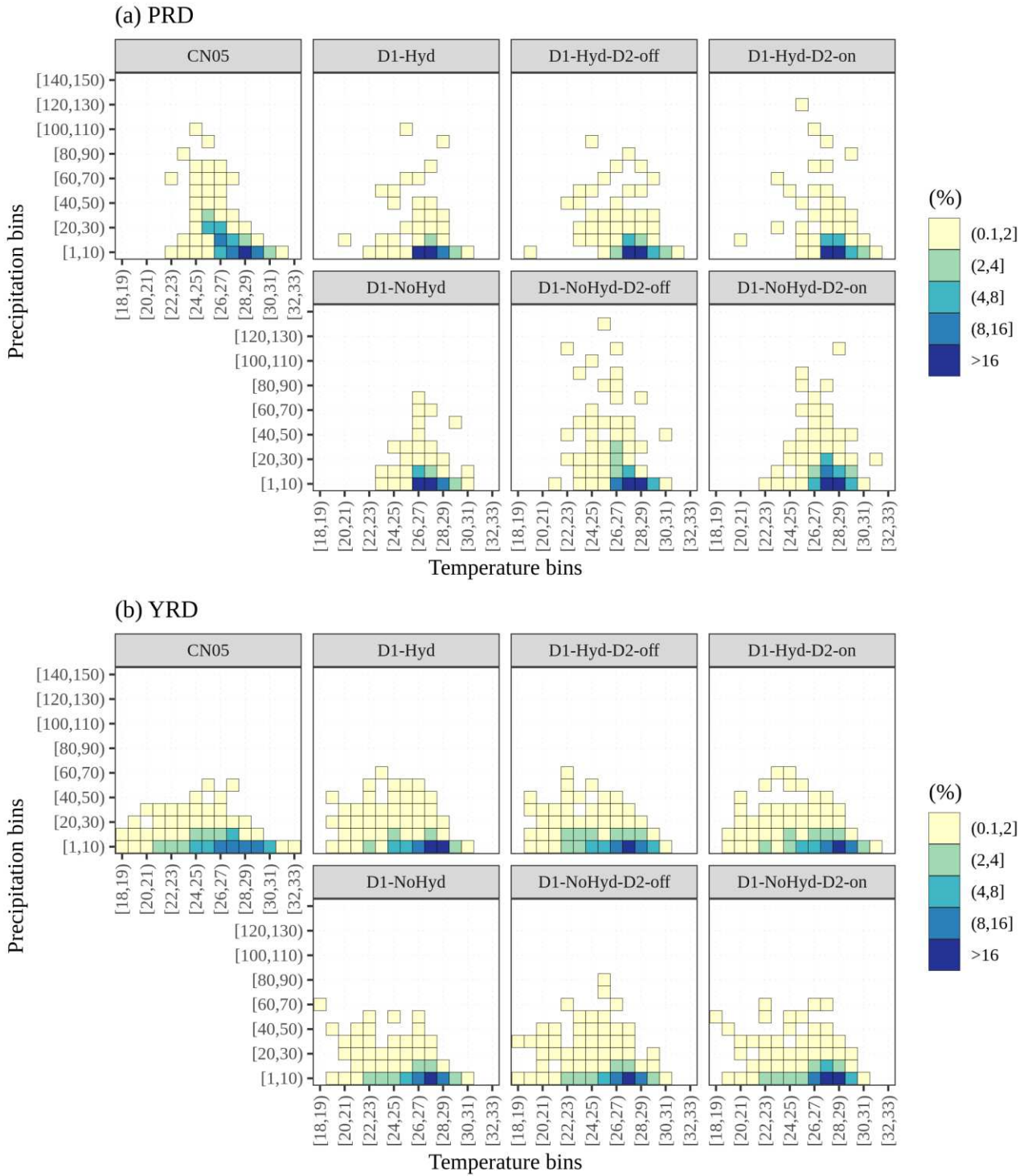
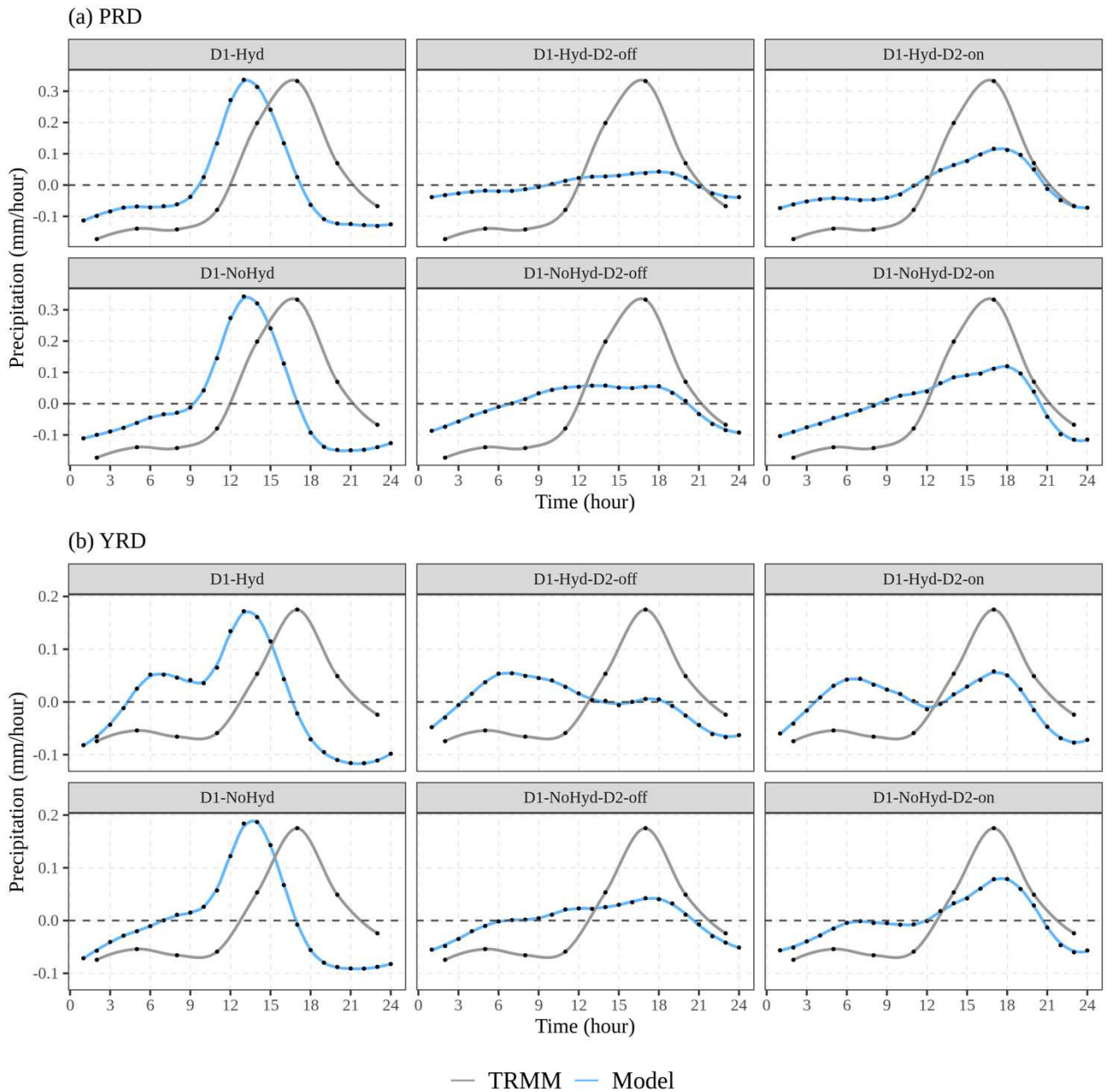
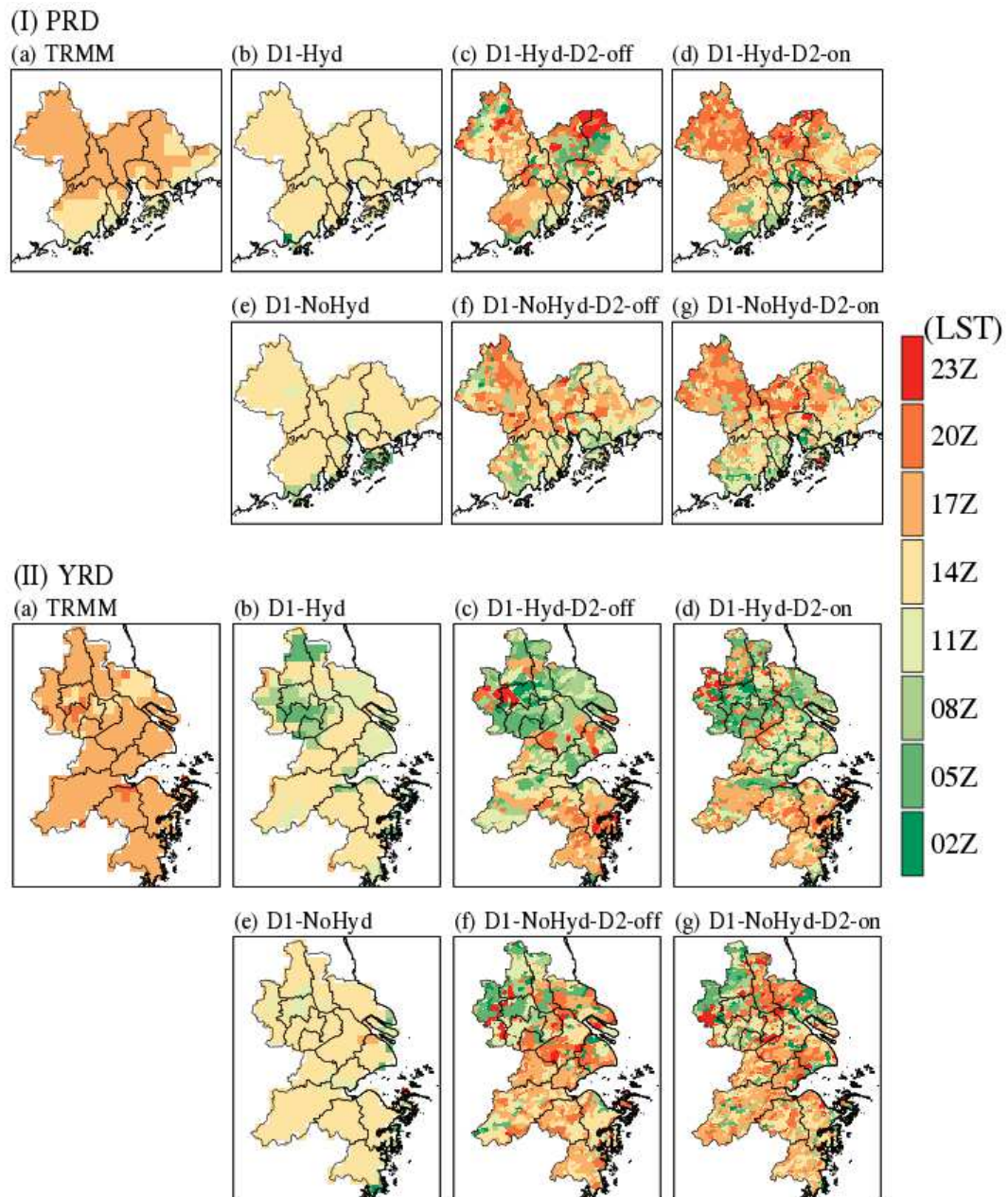


Fig. 6. Joint probability distribution of daily temperature and daily precipitation averaged over (a) PRD and (b) YRD. The different color is proportional to the percentage of corresponding days.



624

625 **Fig. 7.** Anomalous diurnal variation of precipitation rate averaged over the PRD and YRD derived
 626 from TRMM 3-hour observation and 1-hour output of all simulations. Anomalous value at each time
 627 is computed by subtracting daily mean value. The x-axis indicates the local solar time (LST). The
 628 TRMM observation marked by black line is the same in all six panels for (a) PRD and (b) YRD,
 629 respectively.



630

631 **Fig. 8.** The peak timing in the diurnal cycle of precipitation derived from the TRMM observation (a)

632 and all simulations (b-g) for (I) PRD and (II) YRD, respectively.

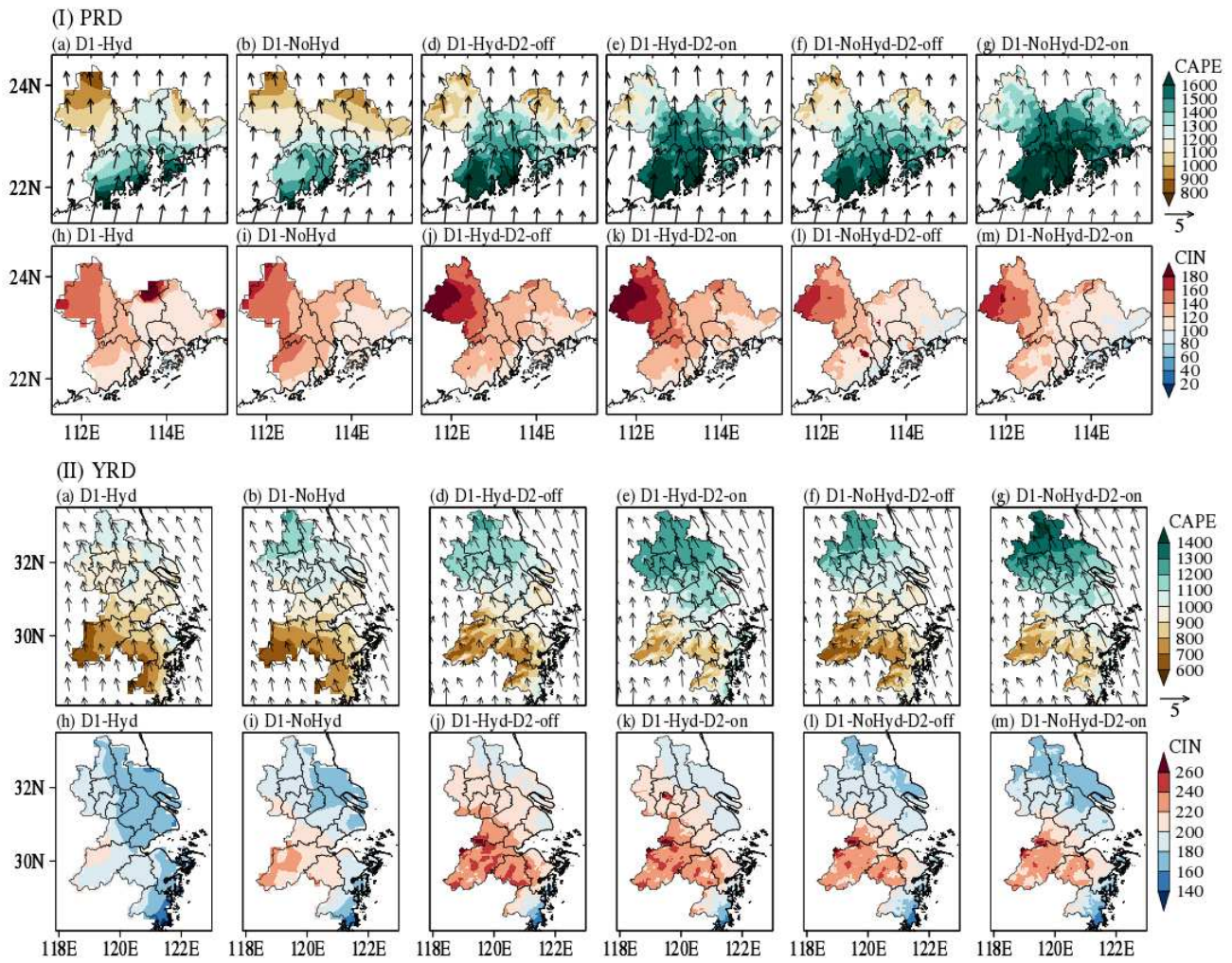


Fig. 9. The spatial distribution of vertically accumulated (a-g) CAPE and (h-m) CIN over (I) PRD and (II) YRD. JJA mean wind vectors are overlaid in the distribution of CAPE.

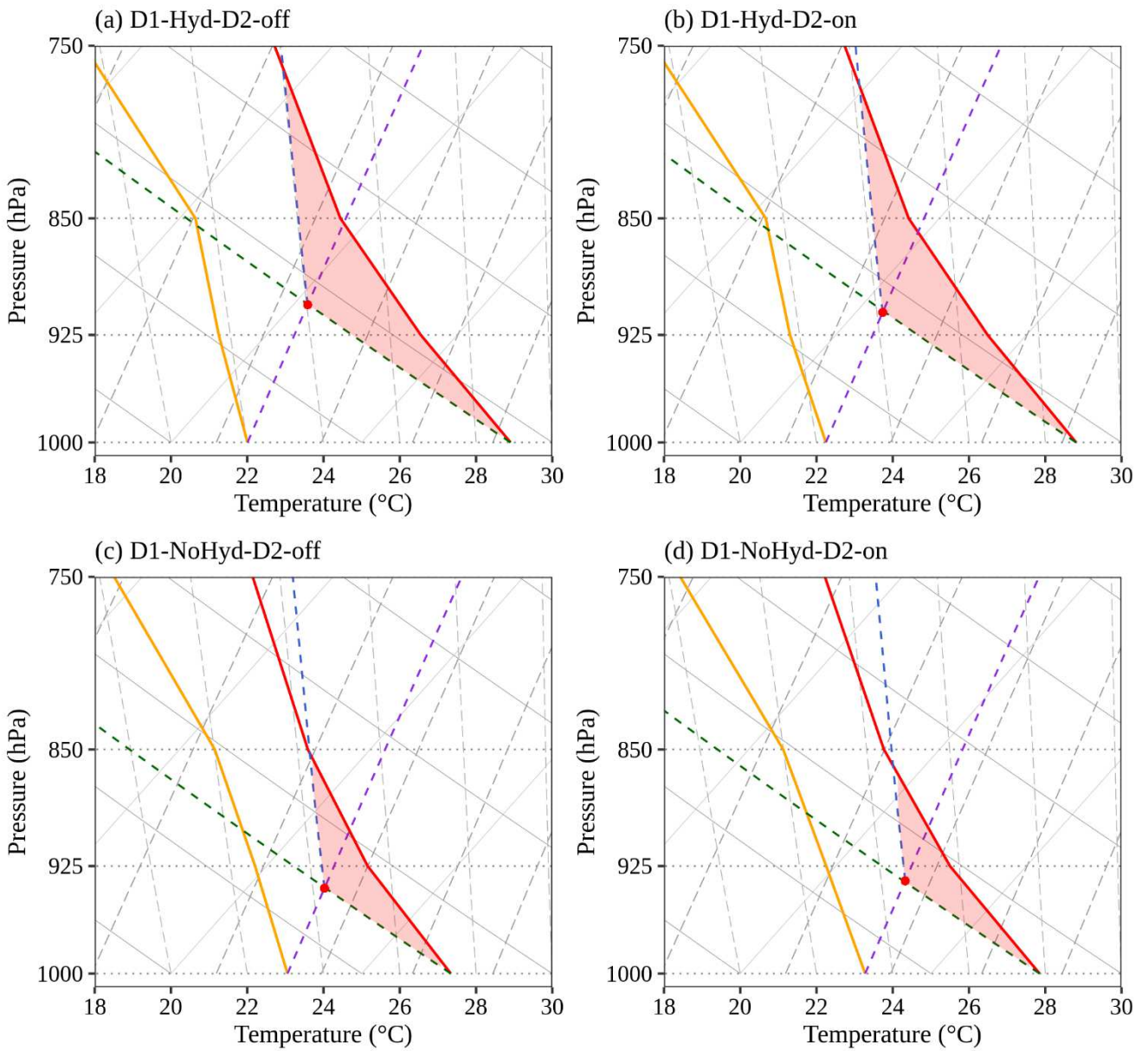


Fig. 10. Skew-T Log-P diagram showing the vertical structure of temperature (T) and dew point temperature (Td) averaged over rectangle in Fig. 1 (b) on July, 2004. While the red and orange solid lines indicate T and Td, respectively, the green, blue and purple dashed lines indicate dry adiabat, moist adiabat, and mixing ratio, respectively. The red dot indicates the lifting condensation level and the shaded area is equivalent to the magnitude of CIN.

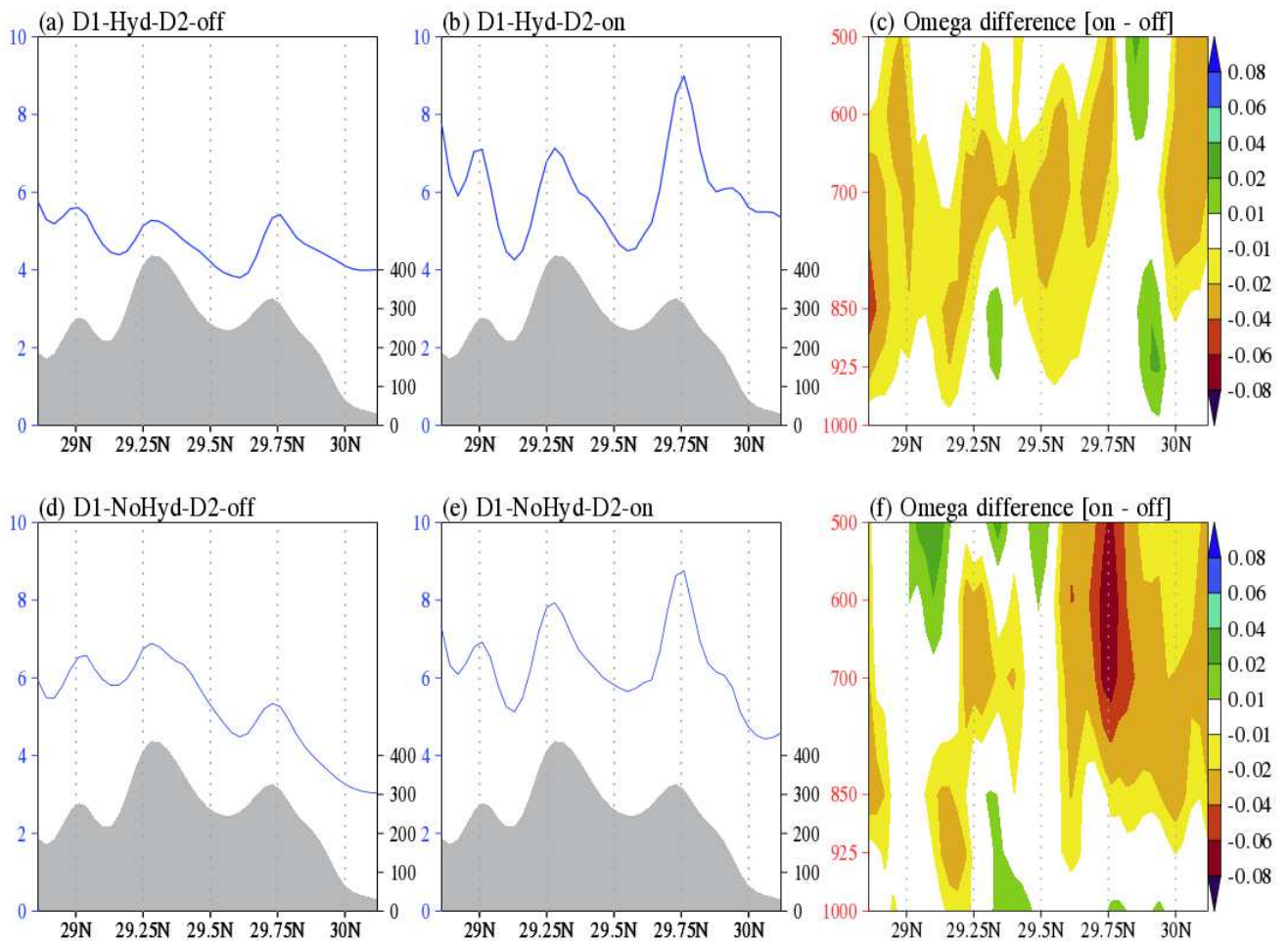


Fig. 11. (a, b, d, e) Latitudinal distribution of precipitation (blue line, unit: mm/day) zonally averaged over 120.86E-121.4E (Fig. 1c) along the south-north topographical transects (grey shading) and (c, f) vertical structure of omega difference (unit: Pa/s) between simulations with CPS on and off.

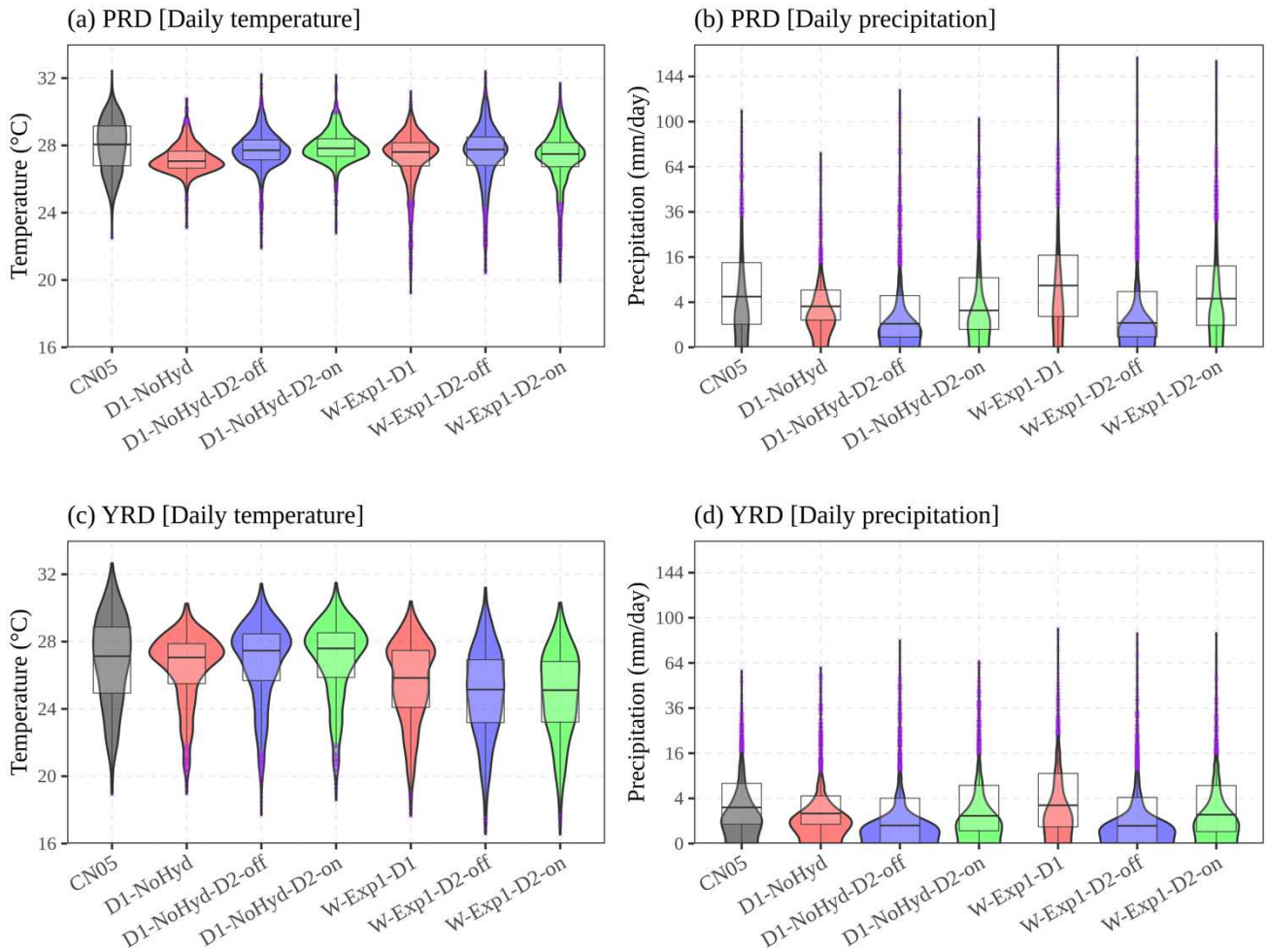


Fig. 12. Violin (shaded) and box plots of (a, c) daily temperature and (b, d) daily precipitation averaged over the PRD and YRD. The y-axis for (b, d) daily precipitation was square-root transformed for better visualization. The distributions of CN05, D1-NoHyd, D1-NoHyd-D2-off, and D1-NoHyd-D2-on are the same with those from Fig. 5.

Figures

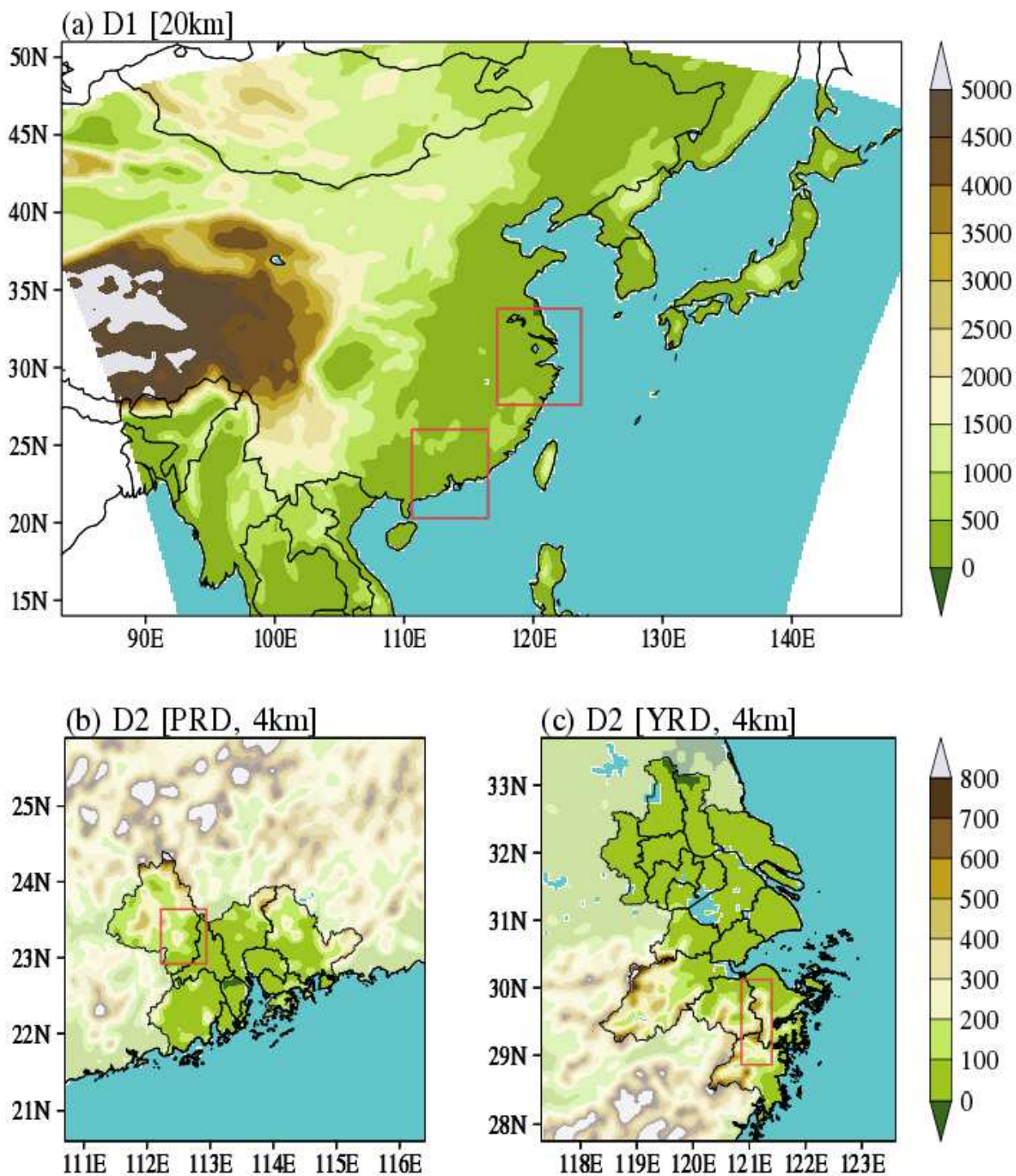


Figure 1

Domain and topography used for the (a) mother domain and (b, c) two nested domains simulations. The geographical locations of two nested domains are marked by red line rectangles in the mother domain. The areas of red line rectangle in (b) and (c) are selected for in-depth analysis presented in Fig. 8 and Fig.

9, respectively. Note: The designations employed and the presentation of the material on this map do not imply the expression of any opinion whatsoever on the part of Research Square concerning the legal status of any country, territory, city or area or of its authorities, or concerning the delimitation of its frontiers or boundaries. This map has been provided by the authors.

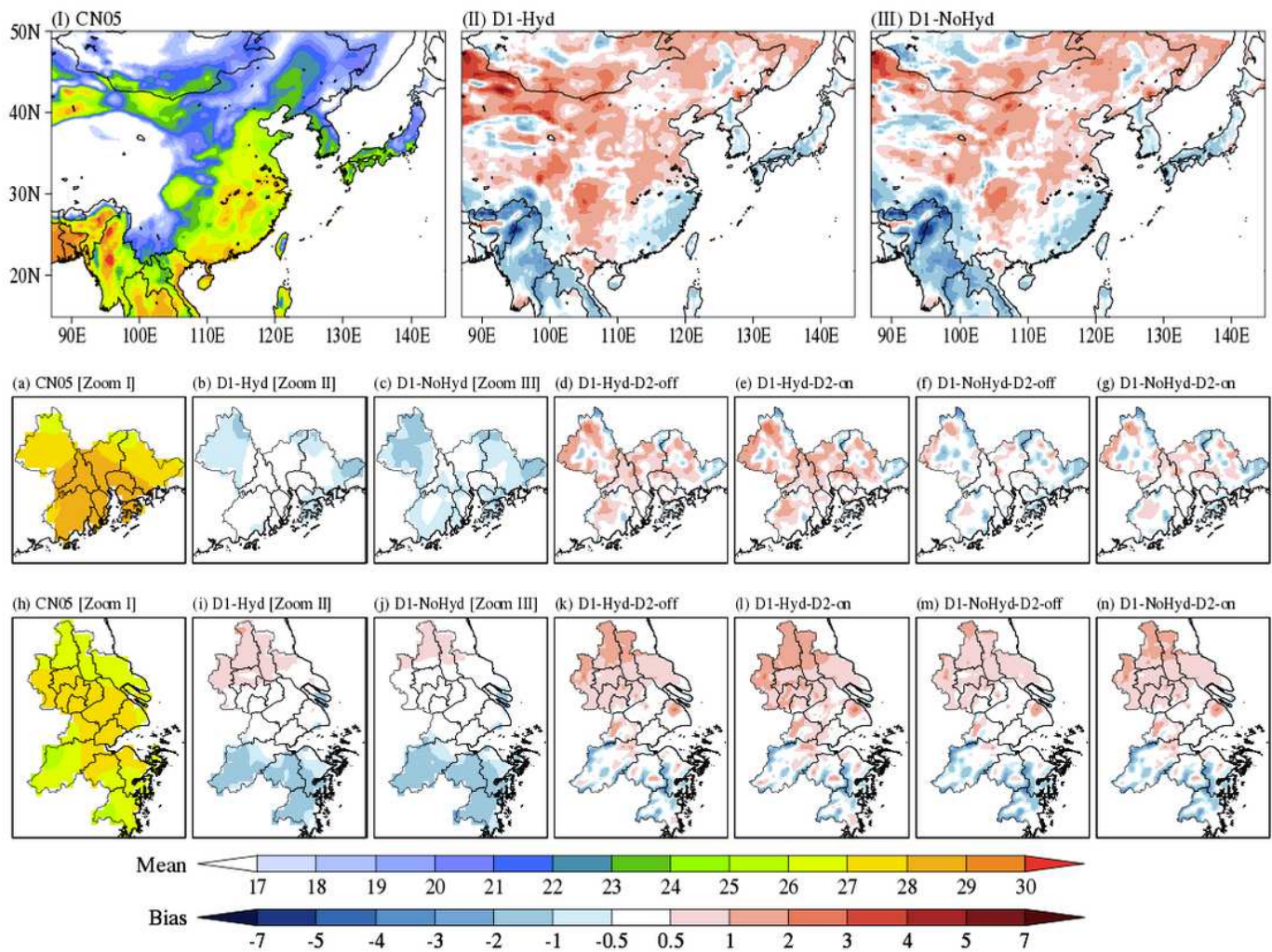


Figure 2

The spatial distributions of (I) JJA mean temperature (unit: °C) from CN05 observation and the bias of JJA mean temperature from (II) D1-Hyd and (III) D1-NoHyd over the whole domain, and the bias of JJA mean temperature over (d-g) PRD and (k-n) YRD from two nested domain simulations with the Emanuel CPS turn on/off driven by (d, e, k, l) D1-Hyd and (f, g, m, n) D1-NoHyd during the 10-year period (2000-2009). The distributions presented in (I), (II), and (III) are zoomed up with respect to (a-c) PRD and (h-j) YRD to facilitate clear comparison with the nested domain simulations. Note: The designations employed and the presentation of the material on this map do not imply the expression of any opinion whatsoever on the part of Research Square concerning the legal status of any country, territory, city or area or of its authorities, or concerning the delimitation of its frontiers or boundaries. This map has been provided by the authors.

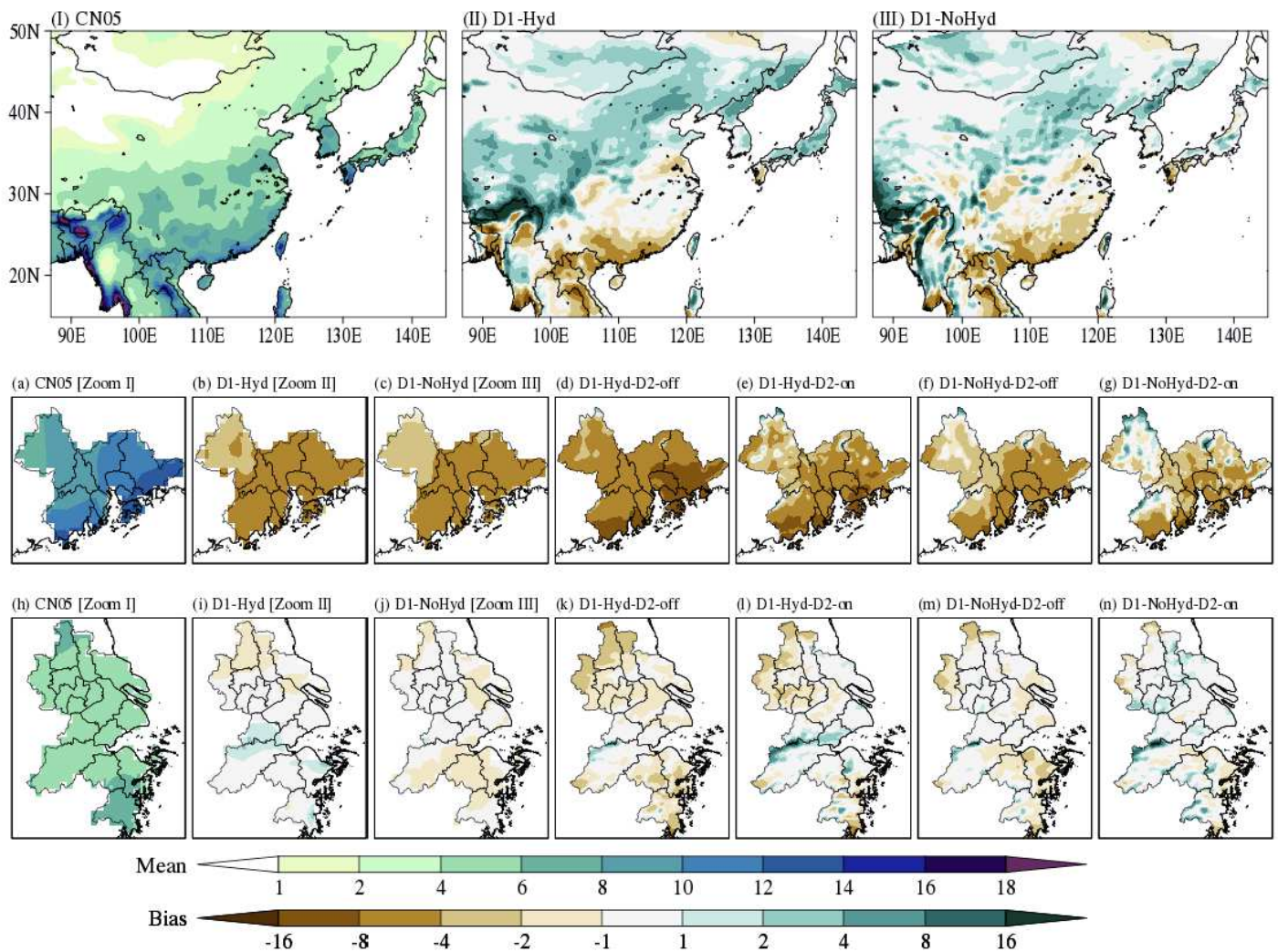
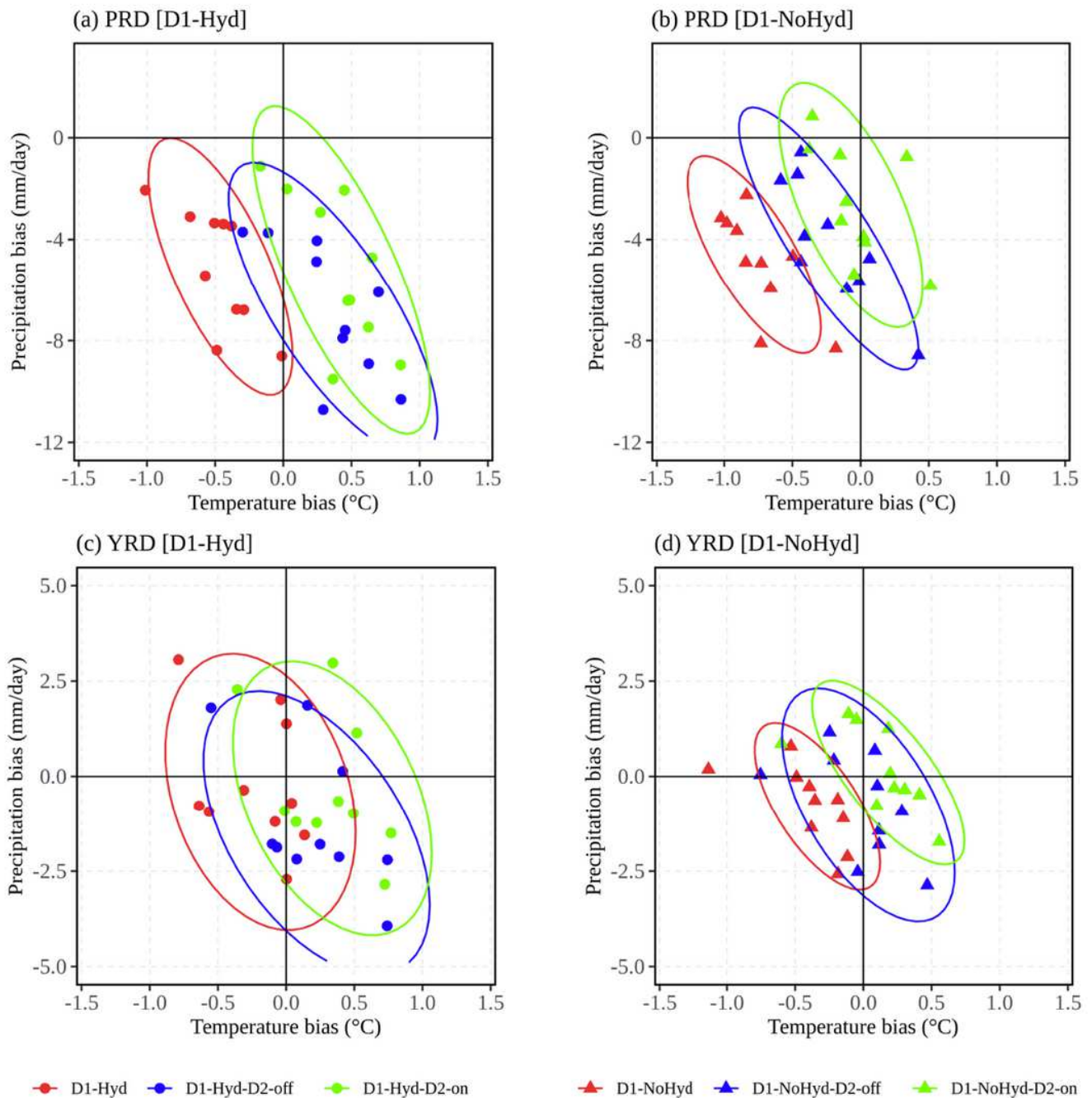


Figure 3

Same as Fig. 2, expect for JJA mean precipitation (unit: mm/day). Note: The designations employed and the presentation of the material on this map do not imply the expression of any opinion whatsoever on the part of Research Square concerning the legal status of any country, territory, city or area or bnbnhjr of its authorities, or concerning the delimitation of its frontiers or boundaries. This map has been provided by the authors.



The ellipses is based on the multivariate t-distribution (confidence level=0.9)

Figure 4

The scatter plot of area-averaged bias of JJA mean temperature and precipitation over (a, b) PRD and (c, d) YRD on a yearly basis. The results from D1-Hyd (D1-NoHyd) and its downscaling simulations are marked as circle (triangle). The ellipses with three different colors indicate the multivariate t-distribution at 0.9 confidence level that is calculated from the corresponding data with the same color.

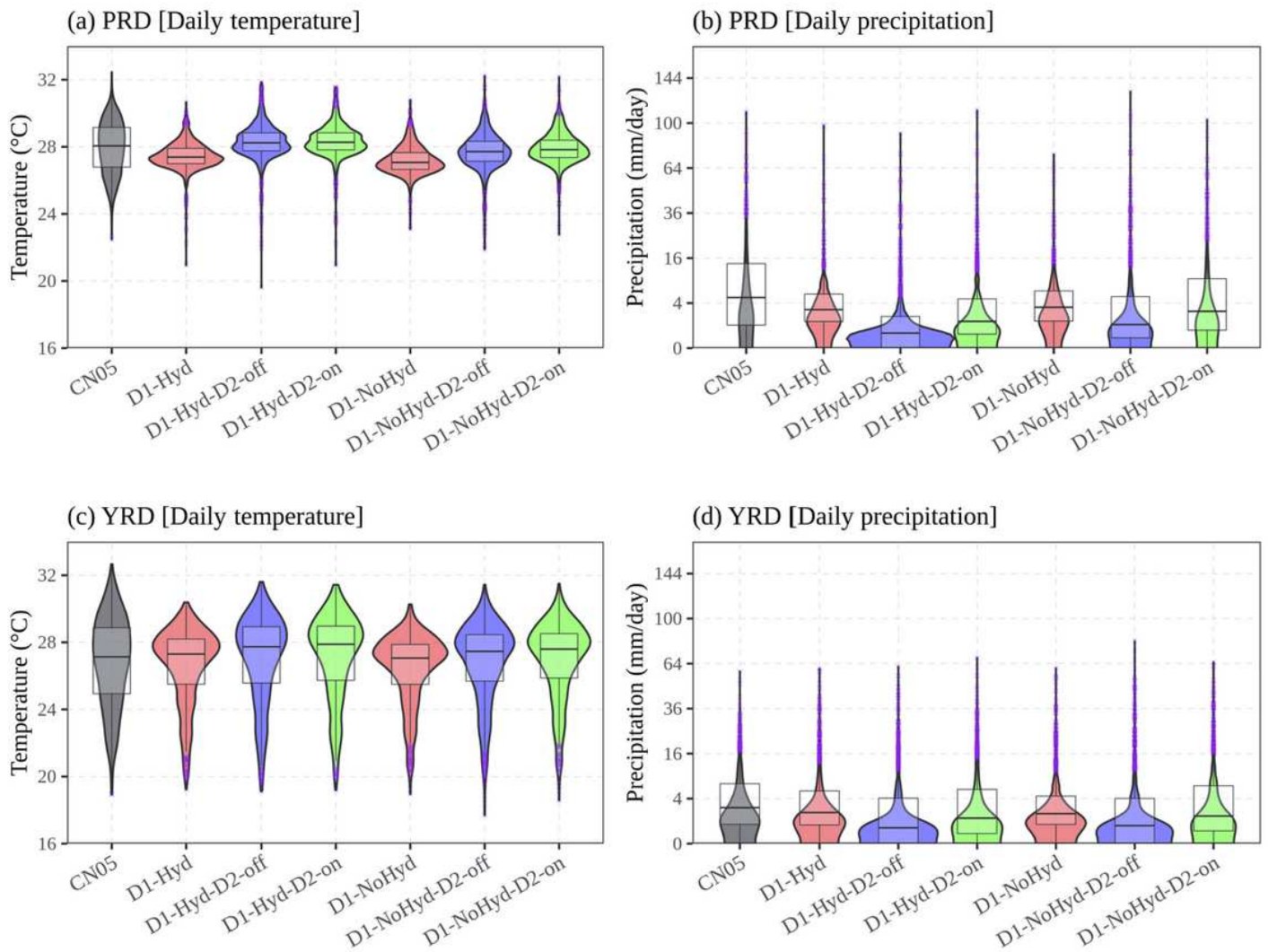


Figure 5

Violin (shaded) and box plots of (a, c) daily temperature and (b, d) daily precipitation averaged over (a, b) PRD and (c, d) YRD. The y-axis for (b, d) daily precipitation was square-root transformed for better visualization.

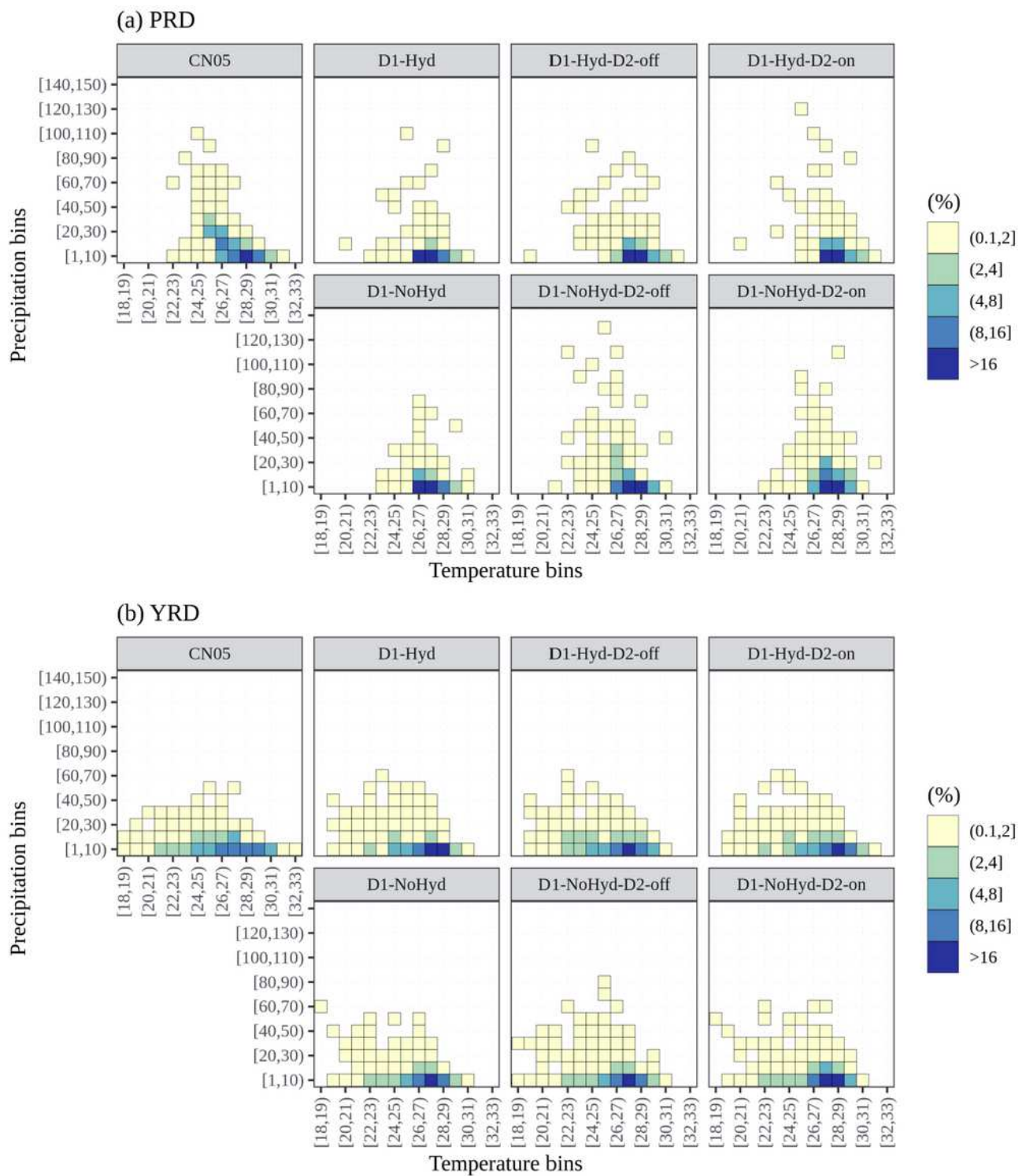


Figure 6

Joint probability distribution of daily temperature and daily precipitation averaged over (a) PRD and (b) YRD. The different color is proportional to the percentage of corresponding days.

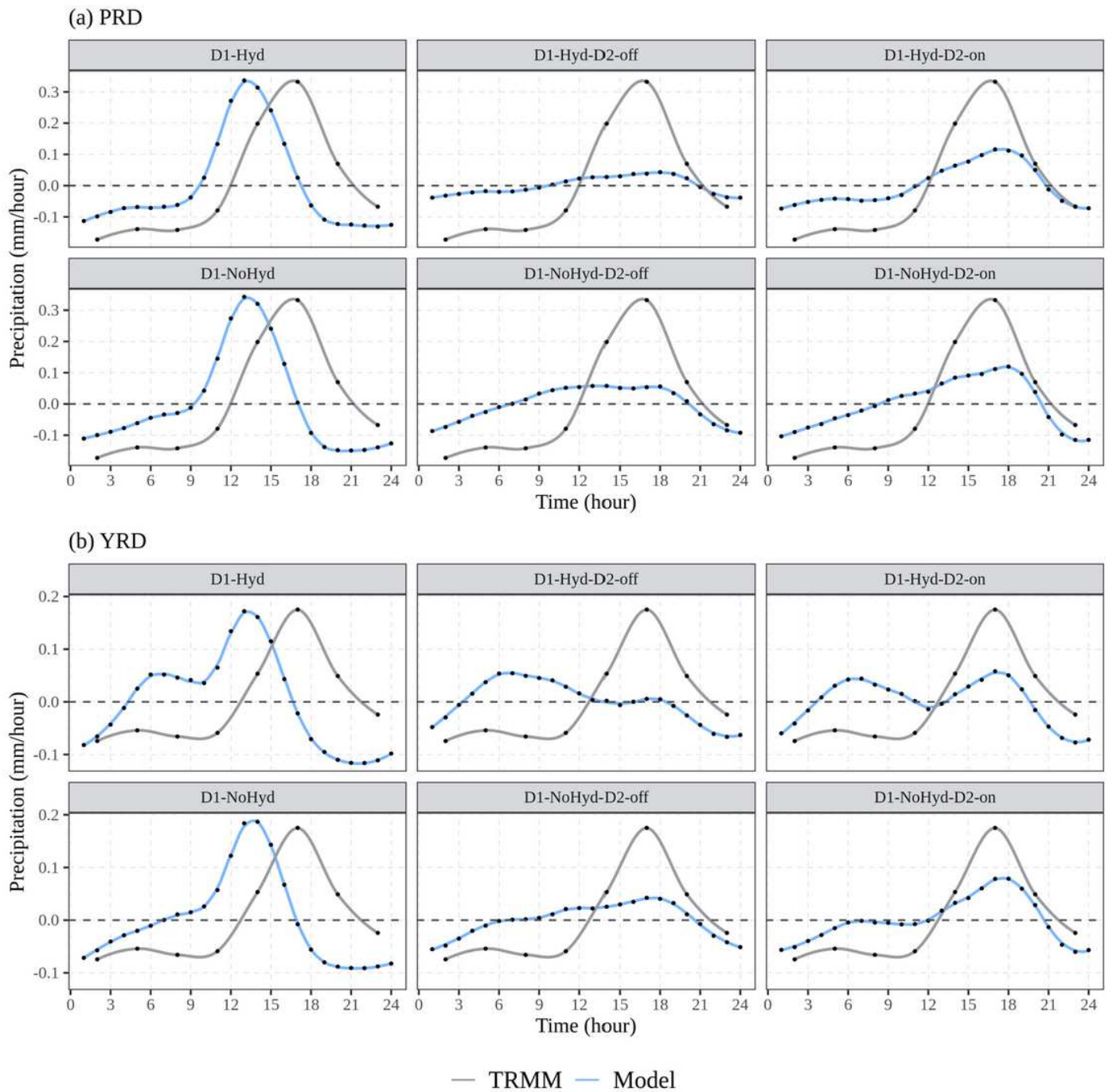


Figure 7

Anomalous diurnal variation of precipitation rate averaged over the PRD and YRD derived from TRMM 3-hour observation and 1-hour output of all simulations. Anomalous value at each time is computed by subtracting daily mean value. The x-axis indicates the local solar time (LST). The TRMM observation marked by black line is the same in all six panels for (a) PRD and (b) YRD, respectively.

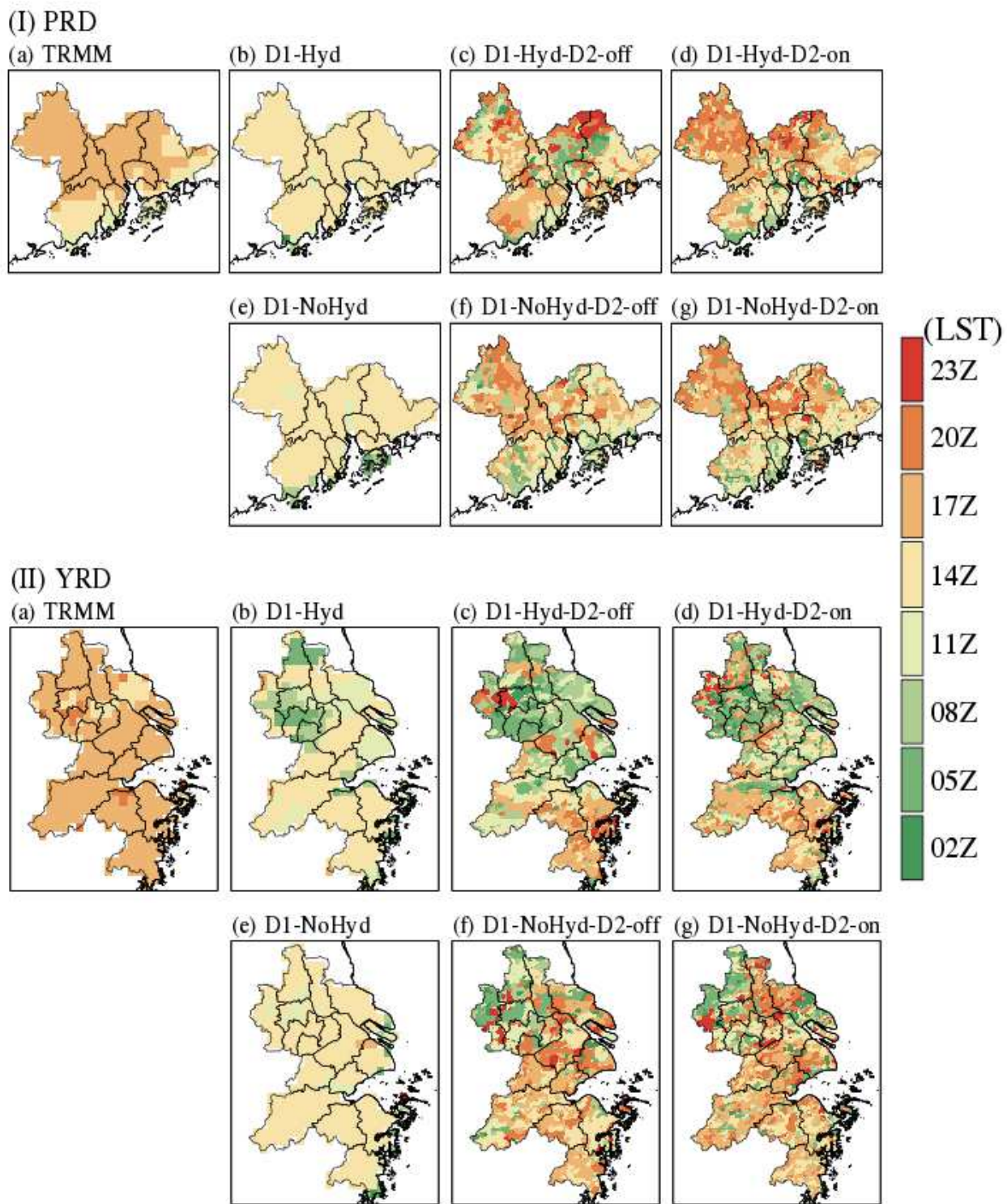


Figure 8

The peak timing in the diurnal cycle of precipitation derived from the TRMM observation (a) and all simulations (b-g) for (I) PRD and (II) YRD, respectively. Note: The designations employed and the presentation of the material on this map do not imply the expression of any opinion whatsoever on the part of Research Square concerning the legal status of any country, territory, city or area or of its

authorities, or concerning the delimitation of its frontiers or boundaries. This map has been provided by the authors.

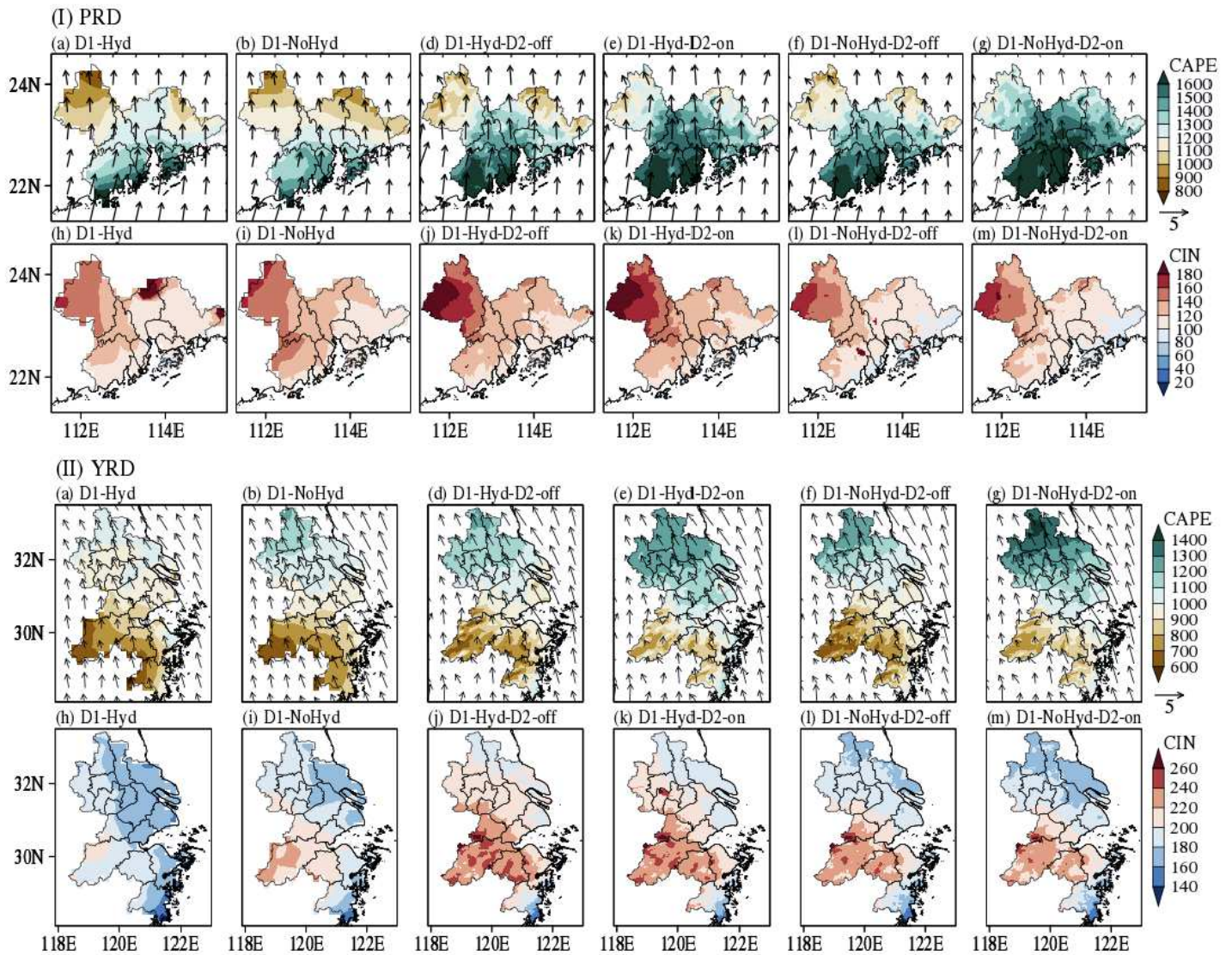


Figure 9

The spatial distribution of vertically accumulated (a-g) CAPE and (h-m) CIN over (I) PRD and (II) YRD. JJA mean wind vectors are overlaid in the distribution of CAPE. Note: The designations employed and the presentation of the material on this map do not imply the expression of any opinion whatsoever on the part of Research Square concerning the legal status of any country, territory, city or area or bbnhjr of its authorities, or concerning the delimitation of its frontiers or boundaries. This map has been provided by the authors.

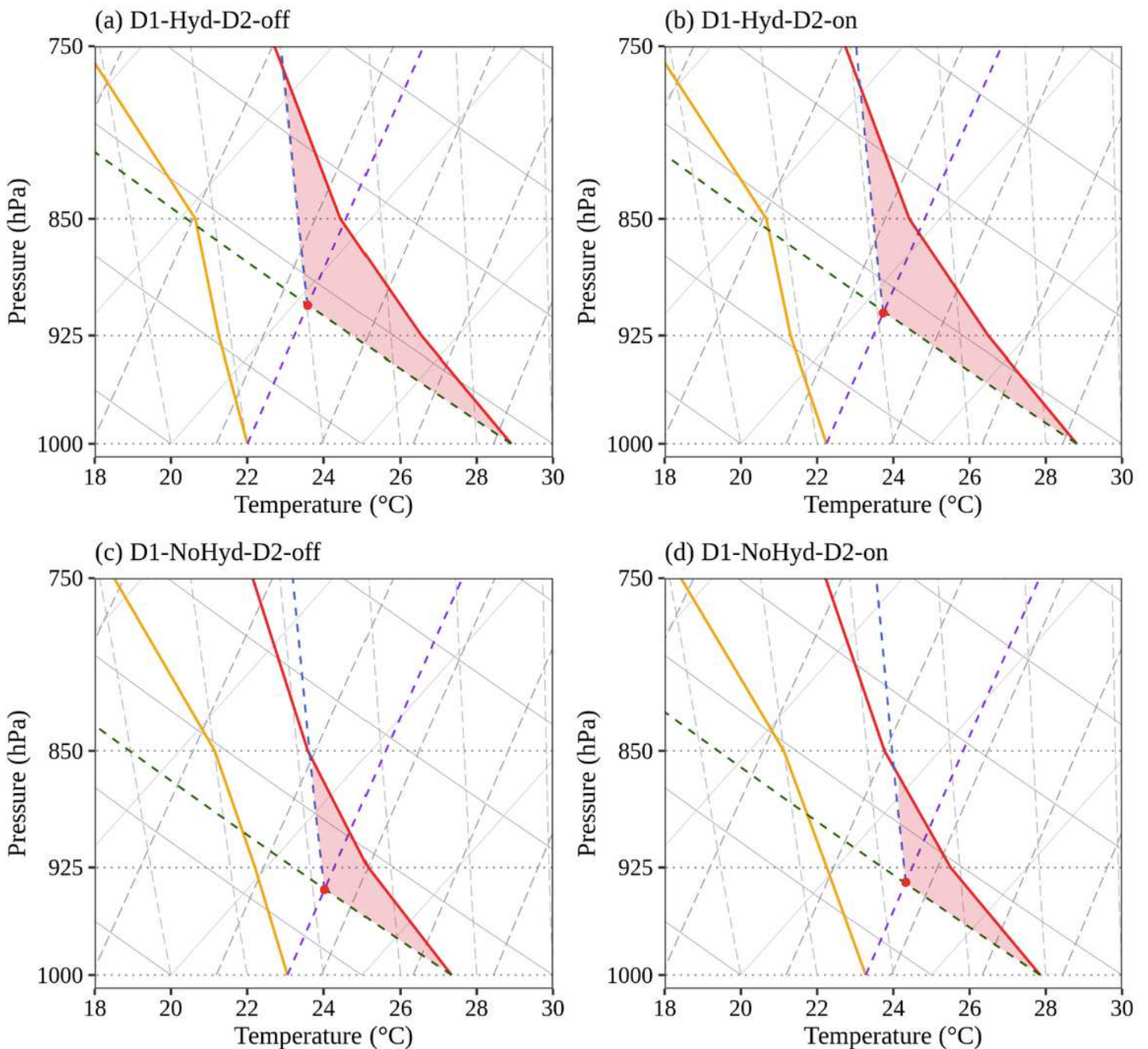


Figure 10

Skew-T Log-P diagram showing the vertical structure of temperature (T) and dew point temperature (T_d) averaged over rectangle in Fig. 1 (b) on July, 2004. While the red and orange solid lines indicate T and T_d , respectively, the green, blue and purple dashed lines indicate dry adiabat, moist adiabat, and mixing ratio, respectively. The red dot indicates the lifting condensation level and the shaded area is equivalent to the magnitude of CIN.

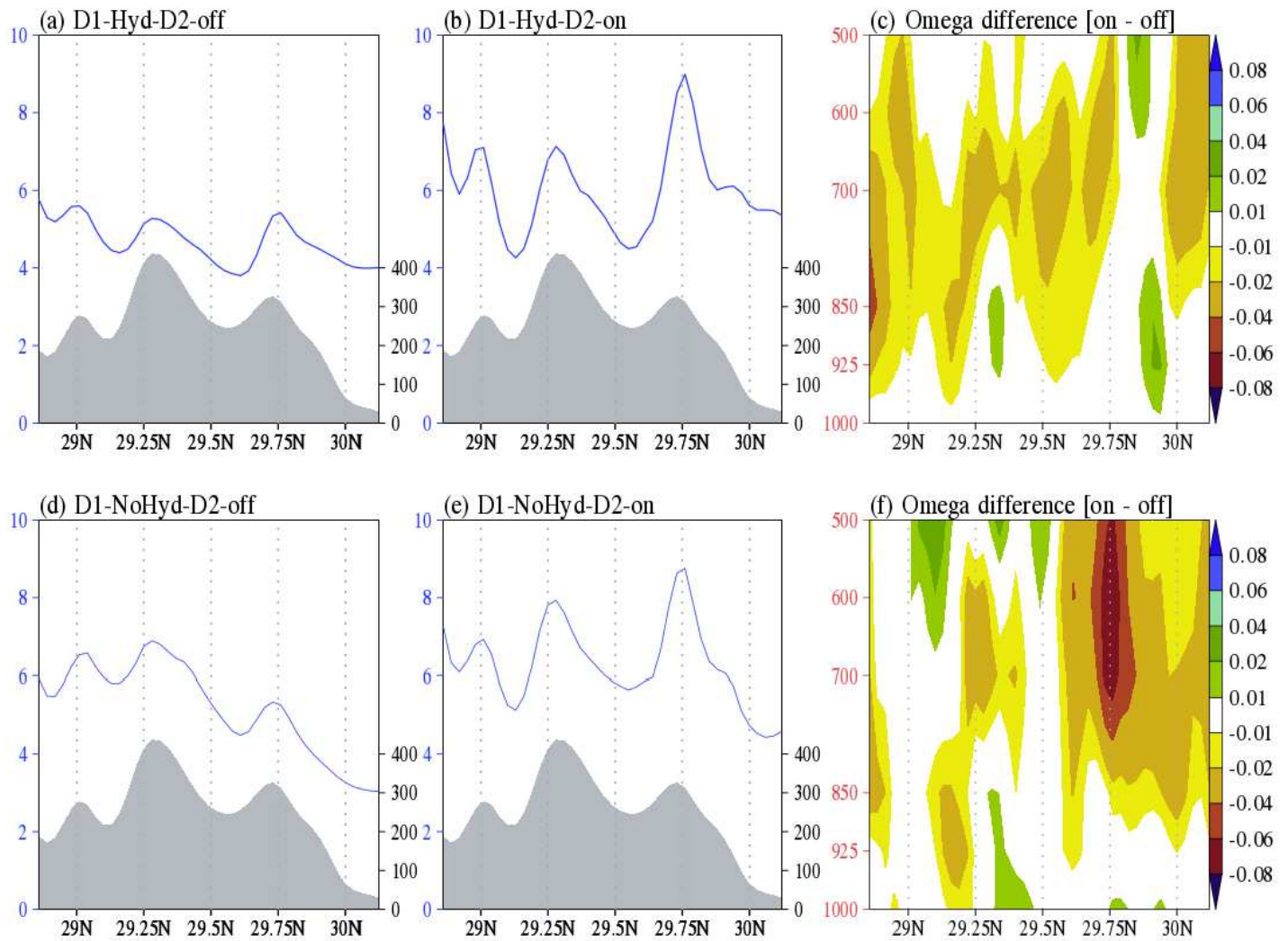


Figure 11

(a, b, d, e) Latitudinal distribution of precipitation (blue line, unit: mm/day) zonally averaged over 120.86E-121.4E (Fig. 1c) along the south-north topographical transects (grey shading) and (c, f) vertical structure of omega difference (unit: Pa/s) between simulations with CPS on and off.

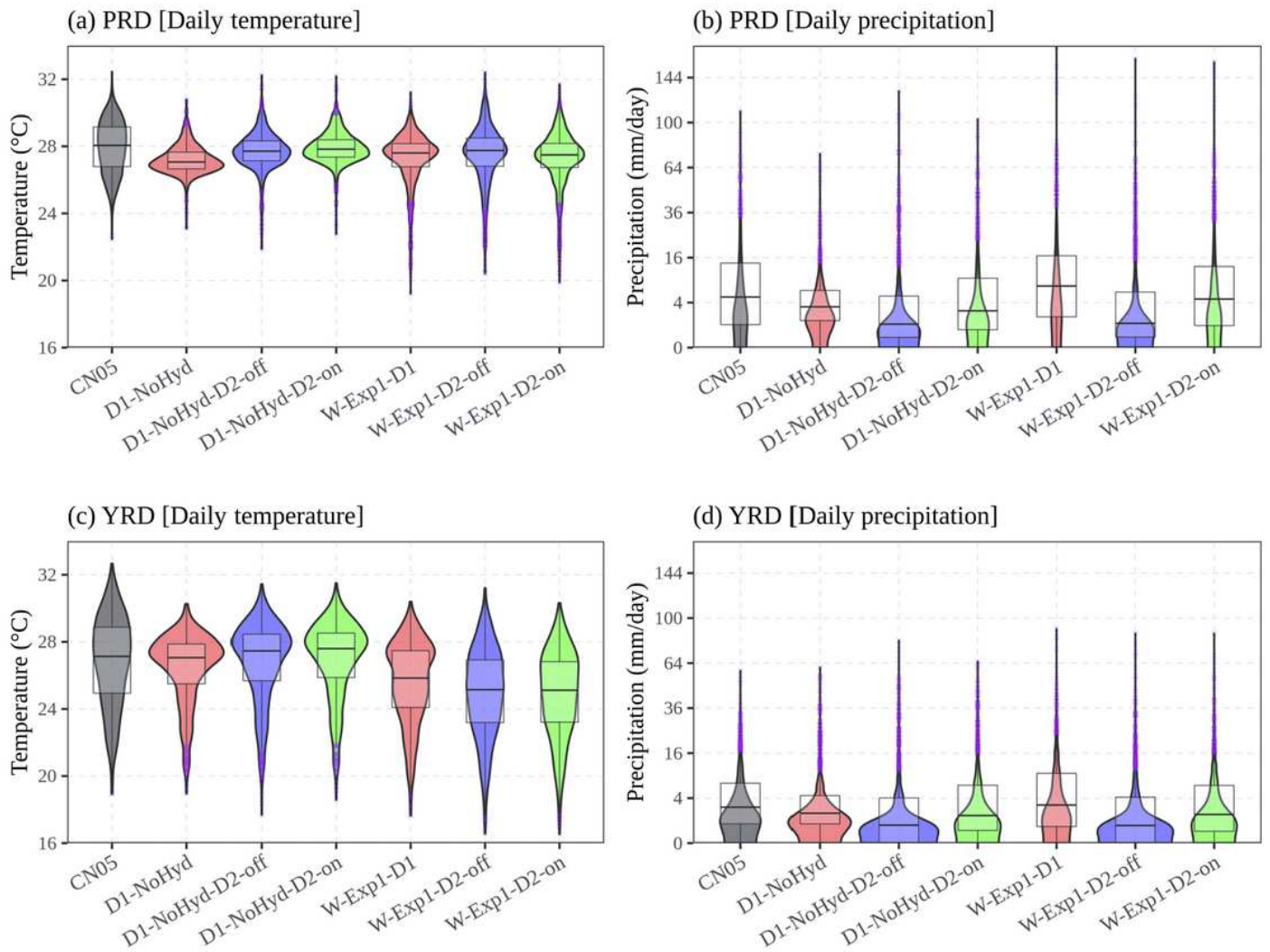


Figure 12

Violin (shaded) and box plots of (a, c) daily temperature and (b, d) daily precipitation averaged over the PRD and YRD. The y-axis for (b, d) daily precipitation was square-root transformed for better visualization. The distributions of CN05, D1-NoHyd, D1-NoHyd-D2-off, and D1-NoHyd-D2-on are the same with those from Fig. 5.

Supplementary Files

This is a list of supplementary files associated with this preprint. Click to download.

- [CDFigSupplFinal.pdf](#)